

1 Components of genetic associations across 2,138 2 phenotypes in the UK Biobank highlight novel adipocyte 3 biology

4
5 Yosuke Tanigawa^{1*}, Jiehan Li^{2,3*}, Johanne Marie Justesen^{1,2,4}, Heiko Horn^{5,6},
6 Matthew Aguirre^{1,7}, Christopher DeBoever^{1,8}, Chris Chang⁹, Balasubramanian Narasimhan^{1,10},
7 Kasper Lage^{5,6,11}, Trevor Hastie^{1,10}, Chong Yon Park², Gill Bejerano^{1,7,12,13}, Erik Ingelsson^{2,3*+},
8 Manuel A. Rivas^{1*+}

- 9 1. Department of Biomedical Data Science, School of Medicine, Stanford University, Stanford, CA, USA.
10 2. Department of Medicine, Division of Cardiovascular Medicine, Stanford University, Stanford, CA, USA.
11 3. Stanford Cardiovascular Institute, Stanford University, Stanford, CA 94305.
12 4. Novo Nordisk Foundation Center for Basic Metabolic Research, Faculty of Health and Medical Sciences,
13 University of Copenhagen, Copenhagen, Denmark
14 5. Department of Surgery, Massachusetts General Hospital, Harvard Medical School, Boston, MA, USA.
15 6. Broad Institute of MIT and Harvard, Cambridge, MA, USA.
16 7. Department of Pediatrics, Stanford University School of Medicine, Stanford University, Stanford, CA, USA.
17 8. Department of Genetics, Stanford University, Stanford, CA, USA.
18 9. Grail, Inc., 1525 O'Brien Drive, Menlo Park, CA, USA.
19 10. Department of Statistics, Stanford University, Stanford, CA, USA.
20 11. Institute for Biological Psychiatry, Mental Health Center Sct. Hans, University of Copenhagen, Roskilde, Denmark.
21 12. Department of Developmental Biology, Stanford University, Stanford, CA, USA.
22 13. Department of Computer Science, Stanford University, Stanford, CA, USA.

23
24 *These authors contributed equally

25 +Corresponding authors

26 Abstract

27 To characterize latent components of genetic associations, we applied truncated singular value
28 decomposition (DeGAs) to matrices of summary statistics derived from genome-wide
29 association analyses across 2,138 phenotypes measured in 337,199 White British individuals in
30 the UK Biobank study. We systematically identified key components of genetic associations and
31 the contributions of variants, genes, and phenotypes to each component. As an illustration of
32 the utility of the approach to inform downstream experiments, we report putative loss of function
33 variants, rs114285050 (*GPR151*) and rs150090666 (*PDE3B*), that substantially contribute to
34 obesity-related traits, and experimentally demonstrate the role of these genes in adipocyte
35 biology. Our approach to dissect components of genetic associations across human phenotypes
36 will accelerate biomedical hypothesis generation by providing insights on previously unexplored
37 latent structures.

38 Introduction

39 Human genetic studies have been profoundly successful at identifying regions of the genome
40 contributing to disease risk^{1,2}. Despite these successes, there are challenges to translating
41 findings to clinical advances, much due to the extreme polygenicity and widespread pleiotropy

42 of complex traits³⁻⁵. In retrospect, this is not surprising given that most common diseases are
43 multifactorial. However, it remains unclear exactly which factors, acting alone or in combination,
44 contribute to disease risk and how those factors are shared across diseases. With the
45 emergence of sequencing technologies, we are increasingly able to pinpoint alleles, possibly
46 rare and with large effects, which may aid in therapeutic target prioritization⁶⁻¹³. Furthermore,
47 large population-based biobanks, such as the UK Biobank, have aggregated data across tens of
48 thousands of phenotypes¹⁴. Thus, an opportunity exists to characterize the phenome-wide
49 landscape of genetic associations across the spectrum of genomic variation, from coding to
50 non-coding, and rare to common.

51 Singular value decomposition (SVD), a mathematical approach developed by differential
52 geometers¹⁵, can be used to combine information from several (likely) correlated vectors to form
53 basis vectors, which are guaranteed to be orthogonal and to explain maximum variance in the
54 data, while preserving the linear structure that helps interpretation. In the field of human
55 genetics, SVD is routinely employed to infer genetic population structure by calculating principal
56 components using the genotype data of individuals¹⁶.

57 To address the pervasive polygenicity and pleiotropy of complex traits, we propose an
58 application of truncated SVD (TSVD), a reduced rank approximation of SVD¹⁷⁻¹⁹, to characterize
59 the underlying (latent) structure of genetic associations using summary statistics computed for
60 2,138 phenotypes measured in the UK Biobank population cohort¹⁴. We applied our novel
61 approach, referred to as DeGAs – Decomposition of Genetic Associations – to assess
62 associations among latent components, phenotypes, variants, and genes. We highlight its
63 application to body mass index (BMI), myocardial infarction (MI), and gallstones, motivated by
64 high polygenicity in anthropometric traits, global burden, and economic costs, respectively. We
65 assess the relevance of the inferred key components through GREAT genomic region ontology
66 enrichment analysis²⁰ and functional experiments. Further, we experimentally demonstrate a
67 role of newly discovered obesity-related genes in adipocyte biology.

68 Results

69 DeGAs method overview

70 We generated summary statistics by performing genome-wide association studies (GWAS) of
71 2,138 phenotypes from the UK Biobank (Fig. 1a, Supplementary Tables S1-S2). We perform
72 variant-level quality control, which includes linkage-disequilibrium (LD) pruning and removal of
73 variants in the MHC region, to focus on 235,907 variants for subsequent analyses. Given the
74 immediate biological consequence, subsequent downstream implications, and medical
75 relevance of predicted protein-truncating variants (PTVs), commonly referred to as loss-of-
76 function variants^{12,21,22}, we perform separate analyses on two variant sets: (1) all directly-
77 genotyped variants and (2) PTVs (Supplementary Fig. S1). To eliminate unreliable estimates of
78 genetic associations, we selected associations with p-values < 0.001, and standard error of beta
79 value or log odds ratio of less than 0.08 and 0.2, respectively, for each dataset. The Z-scores of
80 these associations were aggregated into a summary statistic matrix W of size $N \times M$, where N
81 and M denote the number of phenotypes and variants, respectively. N and M were 2,138 and

82 235,907 for the “all” variant group; and 628 and 784 for the PTV group. The rows and columns
83 of W correspond to the GWAS summary statistics of a phenotype and the phenome-wide
84 association study (PheWAS) of a variant, respectively. We applied TSVD to each matrix and
85 obtained a decomposition into three matrices $W = USV^T$ (U: phenotype, S: variance, V: variant).
86 This reduced representation of $K = 100$ components altogether explained 41.9% (all) and
87 75.5% (PTVs) of the variance in the original summary statistic matrices (Fig. 1b-c, Methods,
88 Supplementary Fig. S2).

89 To characterize each latent component, we defined phenotype squared cosine score,
90 phenotype contribution score, variant contribution score, and gene contribution score. The
91 squared cosine scores quantifies the relative importance of component for a given phenotype or
92 gene, and are defined based on the squared distance of a component from the origin on the
93 latent space²³ (Fig. 1d, Methods). Contribution scores quantify relative importance of a
94 phenotype, variant, or gene to a given component and is defined based on the squared distance
95 of a phenotype, variant, or gene from the origin (Fig. 1d). We then performed biological
96 characterization of DeGAs latent components with the genomic region enrichment analysis tool
97 (GREAT)²⁰ followed by functional experiments in adipocytes (Fig. 1e).

98 Characterization of latent structures of DeGAs

99 The PCA plots show the projection of phenotypes and variants onto DeGAs latent components.
100 (Fig. 2a-b). For the variant plot, we overlay biplot annotation as arrows to interpret the direction
101 of the components (Fig. 2b). Overall, we find that the first five principal components of genetic
102 associations can be attributed to: 1) fat-free mass that accounts for the “healthy part” of body
103 weight²⁴ (32.7%, Supplementary Table S3) and two intronic variants in *FTO* (rs17817449:
104 contribution score of 1.15% to PC1, rs7187961: 0.41%); and a genetic variant proximal to
105 *AC105393.1* (rs62106258: 0.46%); 2) whole-body fat mass (61.5%) and the same three *FTO*
106 and *AC105393.1* variants (rs17817449: 0.97%, rs7187961: 0.28%, rs62106258: 0.27%); 3)
107 bioelectrical impedance measurements (38.7%), a standard method to estimate body fat
108 percentage^{25,26}, and genetic variants proximal to *ACAN* (rs3817428: 0.64%), *ADAMTS3*
109 (rs11729800: 0.31%), and *ADAMTS17* (rs72770234: 0.29%); 4) eye meridian measurements
110 (80.9%), and two intronic variants in *WNT7B* (rs9330813: 5.73%, rs9330802: 1.14%) and a
111 genetic variant proximal to *ATXN2* (rs653178: 0.96%); and 5) bioelectrical impedance and
112 spirometry measures (45.4% and 26.0%, respectively) and genetic variants proximal to *FTO*
113 (rs17817449: 0.17%), *ADAMTS3* (rs11729800: 0.11%), and *PSMC5* (rs13030: 0.11%) (Fig. 2c-
114 d, Supplementary Table S4).

115 Applying DeGAs components for BMI, MI, and gallstones

116 To illustrate the application of DeGAs in characterizing the genetics of complex traits, we
117 selected three phenotypes, BMI, MI, and gallstones given the large contribution of
118 anthropometric traits on the first five components, that ischemic heart diseases is a leading
119 global fatal and non-fatal burden, and that gallstones is a common condition with severe pain
120 and large economic costs where polygenic risk factors are largely unknown^{27,28}. We identified

121 the top three key components for these three phenotypes with DeGAs using the “all” variants
122 dataset.

123 For BMI, we find that the top three components of genetic associations (PC2, PC1, and
124 PC30) altogether explained over 69% of the genetic associations (47%, 18%, and 4%,
125 respectively, Supplementary Fig. S3a). The top two components (PC2 and PC1) corresponded
126 to components of body fat (PC2) and fat-free mass measures (PC1), as described above. PC30
127 was driven by fat mass (28.7%) and fat-free mass (6.8%), but also by non-melanoma skin
128 cancer (7.72%) – linked to BMI in epidemiological studies²⁹ – and childhood sunburn (7.61%)
129 (Fig. 3a, Supplementary Table S4).

130 For MI, a complex disease influenced by multiple risk factors³⁰, we found that the top
131 components were attributed to genetics of lipid metabolism (PC22, high-cholesterol, statin
132 intake, and *APOC1*), alcohol intake (PC100), and sleep duration and food intake (PC83, 25.2%)
133 that collectively corresponded to 36% of the genetic associations (Fig. 3a, Supplementary Fig.
134 S3b, S4-S5, Supplementary Table S4).

135 Cholelithiasis is a disease involving the presence of gallstones, which are concretions
136 that form in the biliary tract, usually in the gallbladder³¹. We found that the top components
137 contributing to gallstones corresponded to associations with fresh fruit (PC72) and water intake
138 (PC64), as well as bioelectrical impedance of whole body (PC67) corresponding to 51% of
139 genetic associations altogether (Fig. 3a, Supplementary Fig. S3c, S4, S6, Supplementary Table
140 S4).

141 Biological characterization of DeGAs components

142 To provide biological characterization of the key components, we applied the genomic region
143 enrichment analysis tool (GREAT)²⁰ to dissect the biological relevance of the identified
144 components with the both coding and non-coding variants. Given the coverage of the manually
145 curated knowledge of mammalian phenotypes, we focused on the mouse genome informatics
146 (MGI) phenotype ontology³². For each key component, we applied GREAT and found an
147 enrichment for the mouse phenotypes consistent with the phenotypic description of our
148 diseases of interest²⁰. The top component for BMI, identified as the body fat measures
149 component (PC2), showed enrichment of several anthropometric terms including abnormally
150 short feet (brachypodia) (MP:0002772, binomial fold = 9.04, $p = 1.3 \times 10^{-23}$), increased birth
151 weight (MP:0009673, fold = 6.21, $p = 1.3 \times 10^{-11}$), and increased body length (MP:0001257,
152 binomial fold = 3.01, $p = 1.3 \times 10^{-36}$) (Fig. 3B, Supplementary Table S5). For MI, we found
153 enrichment of cardiac terms, such as artery occlusion (PC22, MP:0006134, fold = 15.86, $p =$
154 1.14×10^{-25}) and aortitis (PC22, MP:0010139, aorta inflammation, fold = 9.36, $p =$
155 3.41×10^{-31}) (Supplementary Fig. 7, Supplementary Table S6). Similarly, for gallstones, the
156 top enrichment was for abnormal circulating phytosterol level (PC72, MP:0010075, fold = 11.54,
157 $p = 5.51 \times 10^{-11}$), which is known to be involved in gallstone development³³ (Supplementary
158 Fig. 8, Supplementary Table S7).

159 Protein truncating variants

160 Predicted PTVs are a special class of genetic variants with possibly strong effects on gene
161 function^{9,12,21,34}. More importantly, strong effect PTV-trait associations can uncover promising
162 drug targets, especially when the direction of effect is consistent with protection of human
163 disease. Given the challenges with interpreting genetic associations across thousands of
164 possibly correlated phenotypes, we applied DeGAs to PTV gene-phenotype associations. We
165 identified PC1 and PC3 as the top two key components for BMI, with 28% and 12% of
166 phenotype squared contribution scores, respectively (Supplementary Fig. S9). The major drivers
167 of PC1 were weight-related measurements, including left and right leg fat-free mass (5.0% and
168 3.7% of phenotype contribution score for PC1, respectively), left and right leg predicted mass
169 (4.9% each), weight (4.6%), and basal metabolic rate (4.6%), whereas the drivers of PC3
170 included standing height (13.7%), sitting height (8.1%), and high reticulocyte percentage (6.4%)
171 (Fig. 4a, Supplementary Table S4). Top contributing PTVs to PC1 included variants in *PDE3B*
172 (19.0%), *GPR151* (12.3%), and *ABTB1* (8.5%), whereas PC3 was driven by PTVs on *TMEM91*
173 (8.6%), *EML2-AS1* (6.7%), and *KIAA0586* (6.0%) (Fig. 4b, Supplementary Table S4).

174 Based on stop-gain variants in *GPR151* (rs114285050) and *PDE3B* (rs150090666)
175 being key contributors to the top two components of genetic associations for PTVs and BMI
176 (Fig. 4c), we proceeded to detailed phenome-wide association analysis (PheWAS) assessing
177 associations of these PTVs with anthropometric phenotypes. PheWAS analysis of these
178 variants confirmed strong associations with obesity-related phenotypes including waist
179 circumference (*GPR151*, marginal association beta = -0.065, $p = 2.5 \times 10^{-8}$), whole-body fat
180 mass (*GPR151*, beta = -0.069, $p = 1.4 \times 10^{-7}$), trunk fat mass (*GPR151*, beta = -0.071, $p =$
181 1.5×10^{-7}), hip circumference (*PDE3B*, beta = 0.248, $p = 1.8 \times 10^{-11}$), right leg fat-free mass
182 (*PDE3B*, beta = 0.129, $p = 4.2 \times 10^{-8}$) and body weight (*PDE3B*, beta = 0.177, $p = 4.6 \times 10^{-8}$)
183 (Fig. 4d, Supplementary Fig. S10, Supplementary Table S8-9). Among 337,199 White British
184 individuals, we found 7,560 heterozygous and 36 homozygous carriers of the *GPR151* variant
185 and 947 heterozygous carriers of *PDE3B* variants. To assess the effect of the PTVs on BMI, a
186 commonly-used measure of obesity, we performed univariate linear regression analysis with
187 age, sex, and the first four genetic PCs as covariates and found that heterozygous and carriers
188 of *GPR151* PTVs showed 0.324 kg/m² lower BMI than the average UK Biobank participant ($p =$
189 4.13×10^{-7}). We did not find evidence of association with homozygous carriers ($N = 28$; $p =$
190 0.665), presumably due to lack of power (Supplementary Fig. S11). Heterozygous carriers of
191 *PDE3B* PTVs showed 0.647 kg/m² higher BMI ($p = 2.09 \times 10^{-4}$) than the average UK Biobank
192 participant (Supplementary Fig. S12).

193 Functional experiments for candidate genes in cellular models of 194 adipocytes

195 We sought to illustrate the potential application of DeGAs in prioritizing therapeutic targets using
196 functional follow-up experiments. Several of our most interesting findings were observed for
197 obesity-related traits, including the top two candidate genes (*PDE3B* and *GPR151*) contributing
198 to PC1 – the leading component associated with obesity. For this reason, we chose to study
199 these two genes in relation to adipocyte biology. Specifically, the expression and function of

200 *PDE3B* and *GPR151* were evaluated in mouse 3T3-L1 and human Simpson-Golabi-Behmel
201 Syndrome (SGBS) cells, two well-established preadipocyte models used for studying adipocyte
202 differentiation (i.e. adipogenesis) and function^{35,36}.

203 First, we demonstrated that both genes were expressed in preadipocytes, but showed
204 different expression patterns when cells were transforming into mature adipocytes: *PDE3B*
205 increased dramatically during both mouse and human adipogenesis, while *GPR151* maintained
206 a low expression level throughout the differentiation (Fig. 5a-b). Next, to explore the causal
207 relationships between gene expression and adipogenesis, we introduced short interfering RNA
208 (siRNA) against *Pde3b* and *Gpr151*, respectively, into 3T3-L1 preadipocytes and monitored the
209 impact of gene knockdown on conversion of preadipocytes to adipocytes. Knockdown of
210 *Gpr151* (Fig. 5c) drastically impaired adipocyte differentiation, as evidenced by lowered
211 expression of adipogenesis markers (*Pparg*, *Cebpa* and *Fabp4*) (Fig. 5d), as well as the
212 reduced formation of lipid-containing adipocytes (Fig. 5e-f). Further, to test the functional
213 capacity of the fat cells lacking *Gpr151*, we performed a lipolysis assay - an essential metabolic
214 pathway of adipocytes and thus, a key indicator of adipocyte function - on mature adipocytes
215 derived from preadipocytes transfected with either scrambled siRNA (scRNA) or si*Gpr151*. Not
216 surprisingly, *Gpr151*-deficient lipid-poor adipocytes showed dramatically lower lipolysis, along
217 with impaired capability of responding to isoproterenol (ISO), a β -adrenergic stimulus of lipolysis
218 (Fig. 5g). These data suggest that *GPR151* knockdown in adipocyte progenitor cells may block
219 their conversion into mature adipocytes; thus, preventing the expansion of adipose tissue.
220 These results are directionally consistent with our DeGAs and univariate regression analysis
221 showing that *GPR151* PTVs are associated with lower obesity and fat mass, especially central
222 obesity (e.g. waist circumference and trunk fat mass) (Fig. 4d).

223 To further analyze the functional impact of GPR151 in adipocytes, we generated an
224 overexpression model of GPR151 by infecting 3T3-L1 preadipocytes with virus expressing Flag-
225 tagged human *GPR151* driven by either EF1 α or aP2 promotor (Supplementary Fig. S13a).
226 Overexpression of *GPR151* by both constructs were confirmed at the gene and protein levels
227 (Supplementary Fig. S13b-d). However, despite the substantial effect of *Gpr151* knockdown on
228 adipogenesis (Fig. 5), overexpression of *GPR151* in preadipocytes failed to influence adipocyte
229 differentiation significantly, as shown by similar levels of adipogenic markers compared to the
230 non-infected controls (Supplementary Fig. S13e-f). To eliminate the potential masking effects of
231 any unperturbed cells in the partially infected cell population, we specifically selected *GPR151*-
232 overexpressing cells by staining Flag-*GPR151* positive cells with APC-conjugated flag antibody
233 (Supplementary Fig. S13g-h) and sorted APC+ and APC- cells from the differentiating adipocyte
234 cultures. In both EF1 α - and aP2-driven *GPR151* overexpression models, *GPR151* mRNA levels
235 were enriched in APC+ cells compared to APC- cells. However, APC+ cells expressed genes
236 characteristics of differentiating adipocytes in a similar level to that of APC- cells
237 (Supplementary Fig. S13i-j). These data conclude that overexpression of GPR151 in
238 preadipocytes cannot further enhance adipogenesis, suggesting that the endogenous level of
239 GPR151 in preadipocytes may be sufficient to maintain the normal differentiation potential of
240 preadipocytes. Although GPR151 is predominantly expressed in the brain, especially in
241 hypothalamic neurons that control appetite and energy expenditure³⁷, we identified for the first
242 time that the GPR151 protein is present in both subcutaneous and visceral adipose tissue from
243 mice (SAT and VAT), albeit in a very low level (Supplementary Fig. S13k). Together with our

244 gain- and loss-of-function studies of *GPR151* in preadipocyte models, we infer that the
245 regulatory role of *GPR151* in body weight may involve both central and peripheral effects. The
246 minimal but indispensable presence of GPR151 in adipose progenitor cells in generating lipid-
247 rich adipocytes seems to represent an important mechanism by which GPR151 promotes
248 obesity.

249 In contrast to *GPR151*, knockdown of *Pde3b* in 3T3-L1 preadipocytes (Supplementary
250 Fig. S14a) showed no significant influence on adipogenesis and lipolysis (under either basal or
251 β -adrenergic stimulated conditions), as compared to scRNA-transfected controls
252 (Supplementary Fig. S14b-e). Since PDE3B is expressed primarily in differentiated adipocytes
253 (Fig. 5a-b), future research efforts should be concentrated on studying the metabolic role of
254 PDE3B in mature adipocytes. As an essential enzyme that hydrolyzes both cAMP and cGMP,
255 PDE3B is known to be highly expressed in tissues that are important in regulating energy
256 homeostasis, including adipose tissue³⁸. *Pde3b* whole-body knockout in mice reduces the
257 visceral fat mass³⁹ and confers cardioprotective effects⁴⁰. There is a growing body of evidence
258 that cardiometabolic health is linked to improved body fat distribution (i.e. lower visceral fat,
259 higher subcutaneous fat) in a consistent direction⁴¹. Our PheWAS analysis suggests that
260 *PDE3B* PTVs have the strongest association with subcutaneous and lower-body adiposity (e.g.
261 hip and leg fat mass) (Supplementary Fig. S10). Therefore, understanding the fat depot-specific
262 metabolic effects of PDE3B may help uncover the mechanism underlying the positive
263 relationship of *PDE3B* PTVs with peripheral fat accumulation and favorable metabolic profiles.

264 Discussion

265 We developed DeGAs, an application of TSVD, to decompose genome-and phenome-wide
266 summary statistic matrix from association studies of thousands of phenotypes for systematic
267 characterization of latent components of genetic associations. Applying DeGAs, we identified
268 key latent components characterized with disease outcomes, risk factors, comorbidity
269 structures, and environmental factors, with corresponding sets of genes and variants, providing
270 insights on their context specific functions. With additional biological characterization of latent
271 components using GREAT, we find enrichment of relevant phenotypes in mouse phenotype
272 ontology. This replication across species highlights the ability of DeGAs to capture functionally
273 relevant sets of both coding and non-coding variants in each component.

274 Given that DeGAs is applied on summary statistics and does not require individual level
275 data, there is substantial potential to dissect genetic components of the human phenome when
276 applied to data from population-based biobanks around the globe^{14,42-45}. As a proof of concept,
277 we report novel potential therapeutic targets against obesity or its complications based on
278 combination of quantitative results from DeGAs, phenome-wide analyses in the UK Biobank,
279 and functional studies in adipocytes.

280 Taken together, we highlight the directional concordance of our experimental data with
281 the quantitative results from DeGAs and PTV-phenotype associations: *GPR151* inhibition may
282 reduce total body and central fat, while deletion of *PDE3B* may favor subcutaneous, rather than
283 visceral, fat deposition; both are expected to have beneficial effects on cardiometabolic health.
284 Although these two genes were recently reported to be associated with obesity in another
285 recent study based on the UK Biobank⁴⁶, we are the first to experimentally identify *GPR151* as a

286 promising therapeutic target to treat obesity, partly due to its requisite role in regulating
287 adipogenesis. We also suggest *PDE3B* as a potential target of adipocyte-directed therapy. In
288 this study, we focused on evaluating the functional effects of these genes on adipocyte function
289 and development. We do not exclude the contribution nor the importance of other tissues or
290 mechanisms underlying body weight changes. Indeed, some lines of evidence support
291 additional effects of *GPR151* on obesity via the central nervous system – possibly on appetite
292 regulation³⁷.

293 The resource made available with this study, including the DeGAs app, an interactive
294 web application in the Global Biobank Engine⁴⁷, provides a starting point to investigate genetic
295 components, their functional relevance, and new therapeutic targets. These results highlight the
296 benefit of comprehensive phenotyping on a population and suggest that systematic
297 characterization and analysis of genetic associations across the human phenome will be an
298 important part of efforts to understand biology and develop novel therapeutic approaches.

299 Methods

300 Study population

301 The UK Biobank is a population-based cohort study collected from multiple sites across the
302 United Kingdom. Information on genotyping and quality control has previously been described¹⁴.
303 In brief, study participants were genotyped using two similar arrays (Applied Biosystems UK
304 BiLEVE Axiom Array (807,411 markers) and the UK Biobank Axiom Array (825,927 markers)),
305 which were designed for the UK Biobank study. The initial quality control was performed by the
306 UK Biobank analysis team and designed to accommodate the large-scale dataset of ethnically
307 diverse participants, genotyped in many batches, using two similar novel arrays¹⁴.

308 Genotype data preparation

309 We used genotype data from the UK Biobank dataset release version 2¹⁴ and the hg19 human
310 genome reference for all analyses in the study. To minimize the variabilities due to population
311 structure in our dataset, we restricted our analyses to include 337,199 White British individuals
312 based on the following five criteria reported by the UK Biobank in the file “ukb_sqc_v2.txt”:

- 313 1. self- reported white British ancestry (“in_white_British_ancestry_subset” column)
- 314 2. used to compute principal components (“used_in_pca_calculation” column)
- 315 3. not marked as outliers for heterozygosity and missing rates (“het_missing_outliers”
316 column)
- 317 4. do not show putative sex chromosome aneuploidy (“putative_sex_chromo-
318 some_aneuploidy” column)
- 319 5. have at most 10 putative third-degree relatives (“excess_relatives” column).

320
321 We annotated variants using the VEP LOFTEE plugin (<https://github.com/konradjk/loftee>) and
322 variant quality control by comparing allele frequencies in the UK Biobank and gnomAD
323 (gnomad.exomes.r2.0.1.sites.vcf.gz) as previously described¹².

324 We focused on variants outside of major histocompatibility complex (MHC) region
325 (chr6:25477797-36448354) and performed LD pruning using PLINK with "--indep 50 5 2".
326 Furthermore, we selected variants according to the following rules:
327

- Missingness of the variant is less than 1%.
- Minor-allele frequency is greater than 0.01%.
- The variant is in the LD-pruned set.
- Hardy-Weinberg disequilibrium test p-value is greater than 1.0×10^{-7} .
- Manual cluster plot inspection. We investigated cluster plots for subset of our variants
332 and removed 11 variants that has unreliable genotype calls as previously described¹².
- Passed the comparison of minor allele frequency with gnomAD dataset as previously
334 described¹².

335 These variant filters are summarized in Supplementary Fig. S1.

336 Phenotype data preparation

337 We organized 2,138 phenotypes from the UK Biobank in 11 distinct groups (Supplementary
338 Table 1). We included phenotypes with at least 100 cases for binary phenotypes and 100
339 individuals with non-missing values for quantitative phenotypes. For disease outcome
340 phenotypes, cancer, and family history, we used the same definitions as previously described¹².
341 We used specific data fields and data category from the UK Biobank to define the phenotypes in
342 the following categories as well as 19 and 42 additional miscellaneous binary and quantitative
343 phenotypes: medication, imaging, physical measurements, assays, and binary and quantitative
344 questionnaire (Supplementary Table 1-2).

345 Some phenotype information from the UK Biobank contains three instances, each of
346 which corresponds to (1) the initial assessment visit (2006-2010), (2) first repeat assessment
347 visit (2012-2013), and (3) imaging visit (2014-). For binary phenotype, we defined "case" if the
348 participants are classified as case in at least one of their visits and "control" otherwise. For
349 quantitative phenotype, we took a median of non-NA values. In total, we defined 1,196 binary
350 phenotypes and 943 quantitative phenotypes.

351 Genome-wide association analyses of 2,138 phenotypes

352 Association analyses for single variants were applied to the 2,138 phenotypes separately. For
353 binary phenotypes, we performed Firth-fallback logistic regression using PLINK v2.00a (17 July
354 2017) as previously described^{12,48}. For quantitative phenotypes, we applied generalized linear
355 model association analysis with PLINK v2.00a (20 Sep. 2017). We applied quantile
356 normalization for phenotype (--pheno-quantile-normalize option), where we fit a linear model
357 with covariates and transform the phenotypes to normal distribution $N(0, 1)$ while preserving the
358 original rank. We used the following covariates in our analysis: age, sex, types of genotyping
359 array, and the first four genotype principal components computed from the UK Biobank.

360 Summary statistic matrix construction and variant filters

361 We constructed two Z-score summary statistic matrices. Each element of the matrix
362 corresponds to summary statistic for a particular pair of a phenotype and a variant. We imposed
363 different sets of variant filters.

- 364 • Variant quality control filter: Our quality control filter described in the previous section on
365 genotype data preparation.
- 366 • Non-MHC variant filter: All variants outside of major histocompatibility complex region.
367 With this filter, variants in chr6:25477797-36448354 were excluded from the summary
368 statistic matrix.
- 369 • PTVs-only: With this filter, we subset to include only the variants having the VEP
370 LOFTEE predicted consequence of: stop gain, frameshift, splice acceptor, or splice
371 donor.

372 By combining these filters, we defined the following sets of variants

- 373 • All-non-MHC: This is a combination of our variant QC filter and non-MHC filter.
- 374 • PTVs-non-MHC: This is a combination of our variant QC filter, non-MHC filter, and PTVs
375 filter.

376 In addition to phenotype quality control and variant filters, we introduced value-based filters
377 based on statistical significance to construct summary statistic matrices only with confident
378 values. We applied the following criteria for the value filter:

- 379 • P-value of marginal association is less than 0.001.
- 380 • Standard error of beta value or log odds ratio is less than 0.08 for quantitative
381 phenotypes and 0.2 for binary phenotypes.

382 With these filters, we obtained the following two matrices:

- 383 • All-non-MHC dataset that contains 2,138 phenotypes and 235,907 variants. We label
384 this dataset as **“all” dataset**.
- 385 • “PTVs-non-MHC” dataset that contains 628 phenotypes and 784 variants. We label this
386 dataset as **“PTVs only” dataset**. This contains a fewer number of phenotypes because
387 not all the phenotypes have statistically significant associations with PTVs.

388 The effects of variant filters are summarized in Fig. S1. Finally, we transformed the summary
389 statistics to Z-scores so that each vector that corresponds to a particular phenotype has zero
390 mean with unit variance.

391 Truncated singular value decomposition of the summary statistic 392 matrix

393 For each summary statistic matrix, we applied truncated singular value decomposition (TSVD).
394 The matrix, which we denote as W , of size $N \times M$, where N denotes the number of phenotypes
395 and M denotes the number of variants, is the input data. With TSVD, W is factorized into a
396 product of three matrices: U , S , and V^T : $W = USV^T$, where $U = (u_{i,k})_{i,k}$ is an orthonormal
397 matrix of size $N \times K$ whose columns are phenotype (left) singular vectors, S is a diagonal matrix
398 of size $K \times K$ whose elements are singular values, and $V = (v_{j,k})_{j,k}$ is an orthonormal matrix of
399 size $M \times K$ whose columns are variant (right) singular vectors. While singular values in S

400 represent the magnitude of the components, singular vectors in U and V summarizes the
401 strength of association between phenotype and component and variant and component,
402 respectively. With this decomposition, the k -th latent component (principal component, PC k)
403 are represented as a product of k -th column of U , k -th diagonal element in S , and k -th row of
404 V^T . We used implicitly restarted lanczos bidiagonalization algorithm (IRLBA)⁴⁹
405 (<https://github.com/bwlewis/irlba>) implemented on SciDB⁵⁰ to compute the first K components in
406 this decomposition.

407 Relative variance explained by each of the components

408 A scree plot (Fig. S1) quantify the variance explained by each component: variance explained
409 by k -th component = $s_k^2 / \text{Var}_{\text{Tot}}(W)$ where, s_k is the k -th diagonal element in the diagonal matrix
410 S and $\text{Var}_{\text{Tot}}(W)$ is the total variance of the original matrix before DeGAs is applied.

411 Selection of number of latent components in TSVD

412 In order to apply TSVD to the input matrix, the number of components should be specified. We
413 apply $K = 100$ for our analysis for both datasets. We computed the expected value of squared
414 eigenvalues under the null model where the distribution of variance explained scores across the
415 full-ranks are uniform. This can be computed with the rank of the original matrix, which is equal
416 to the number of phenotypes in our datasets:

$$417 \quad E[\text{Variance explained by } k\text{-th component under the null}] = 1 / (\text{Rank}(W)^2)$$

418 For all of the two datasets, we found that that of 100-th component is greater than the
419 expectation. This indicates even the 100-th components are informative to represent the
420 variance of the original matrix. In the interest of computational efficiency, we set $K = 100$.

421 Factor scores

422 From these decomposed matrices, we computed **factor score** matrices for both phenotypes
423 and variants as the product of singular vector matrix and singular values. We denote the one for
424 phenotypes as $F_p = (f_{i,j}^p)_{i,j}$ the one for variants as $F_v = (f_{i,j}^v)_{i,j}$ and defined as follows:

$$425 \quad F_p = US$$
$$426 \quad F_v = VS$$

427 Since these factor scores are mathematically the same as principal components in principal
428 component analysis (PCA), one can investigate the contribution of the phenotypes or variants
429 for specific principal components by simply plotting factor scores²³ (Fig. 2a-b). Specifically,
430 phenotype factor score is the same as phenotype principal components and variant factor score
431 is the same as variant principal components. By normalizing these factor scores, one can
432 compute contribution scores and cosine scores to quantify the importance of phenotypes,
433 variants, and principal components as described below.

434 Scatter plot visualization with biplot annotations

435 To investigate the relationship between phenotype and variants in the TSVD eigenspace, we
436 used a variant of biplot visualization^{51,52}. Specifically, we display phenotypes projected on
437 phenotype principal components ($F_p = US$) as a scatter plot. We also show variants projected on
438 variant principal components ($F_v = VS$) as a separate scatter plot and added phenotype singular
439 vectors (U) as arrows on the plot using sub-axes (Fig. 2b, 4c, S5-6). In scatter plot with biplot
440 annotation, the inner product of a genetic variant and a phenotype represents the direction and
441 the strength of the projection of the genetic association of the variant-phenotype pair on the
442 displayed latent components. For example, when a variant and a phenotype share the same
443 direction on the annotated scatter plot, that means the projection of the genetic associations of
444 the variant-phenotype pair on the displayed latent components is positive. When a variant-
445 phenotype pair is projected on the same line, but on the opposite direction, the projection of the
446 genetic associations on the shown latent components is negative. When the variant and
447 phenotype vectors are orthogonal or one of the vectors are of zero length, the projection of the
448 genetic associations of the variant-phenotype pair on the displayed latent components is zero.
449 Given the high dimensionality of the input summary statistic matrix, we selected relevant
450 phenotypes to display to help interpretation of genetic associations in the context of these traits.

451 Contribution scores

452 To quantify the contribution of the phenotypes, variants, and genes to a given component, we
453 compute **contribution scores**. We first define **phenotype contribution score** and **variant**
454 **contribution score**. We denote phenotype contribution score and variant contribution score for
455 some component k as $\text{cntr}_k^{\text{phe}}(i)$ and $\text{cntr}_k^{\text{var}}(j)$, respectively. They are defined by squaring the
456 left and right singular vectors and normalizing them by Euclidian norm across phenotypes and
457 variants:

$$458 \quad \text{cntr}_k^{\text{phe}}(i) = (u_{i,k})^2$$

$$459 \quad \text{cntr}_k^{\text{var}}(j) = (v_{i,k})^2$$

460 where, i and j denote indices for phenotype and variant, respectively. Because U and V are
461 orthonormal, the sum of phenotype and variant contribution scores for a given component are
462 guaranteed to be one, i.e. $\sum_i \text{cntr}_k^{\text{phe}}(i) = \sum_j \text{cntr}_k^{\text{var}}(j) = 1$.

463 Based on the variant contribution scores for the k -th component, we define the **gene**
464 **contribution score** for some component k as the sum of variant contribution scores for the set
465 of variants in the gene:

$$466 \quad \text{cntr}_k^{\text{gene}}(g) = \sum_{j \in g} \text{cntr}_k^{\text{var}}(j)$$

467 where, g denotes indices for the set of variants in gene g . To guarantee that gene contribution
468 scores for a given component sum up to one, we treat the variant contribution score for the non-
469 coding variants as gene contribution scores. When multiple genes, g_1, g_2, \dots, g_n are sharing the
470 same variants, we defined the gene contribution score for the union of multiple genes rather
471 than each gene:

$$472 \quad \text{cntr}_k^{\text{gene}}(\{g_i \mid i \in [1, n]\}) = \sum_{\{j \mid j \in g_1 \wedge j \in g_2 \wedge \dots \wedge j \in g_n\}} \text{cntr}_k^{\text{var}}(j)$$

473 With these contribution score for a given component, it is possible to quantify the relative
 474 importance of a phenotype, variant, or gene to the component. Since DeGAs identifies latent
 475 components using unsupervised learning, we interpret each component in terms of the driving
 476 phenotypes, variants, and genes, i.e. the ones with large contribution scores for the component.

477 The top 20 driving phenotypes, variants, and genes (based on contribution scores) for
 478 the top five TSVD components and the top three key components for our phenotypes of interest
 479 are summarized in Supplementary Table S3.

480 We used stacked bar plots for visualization of the contribution score profile for each of
 481 the components. We represent phenotypes, genes, or variants with large contribution scores as
 482 colored segments and aggregated contributions from the remaining ones as “others” in the plot
 483 (Fig. 2c-d, 3a, 4a-b, Supplementary Fig. S4). To help interpretation of the major contributing
 484 factors for the key components, we grouped phenotypes into categories, such as “fat”, “fat-free”
 485 phenotypes, and showed the sum of contribution scores for the phenotype groups. The list of
 486 phenotype groups used in the visualization is summarized in Supplementary Table S3.

487 Squared cosine scores

488 Conversely, we can also quantify the relative importance of the latent components for a given
 489 phenotype or variant with **squared cosine scores**. We denote phenotype squared cosine score
 490 for some phenotype i and variant squared cosine score for some variant j as $\cos^2_i^{\text{phe}}(k)$ and
 491 $\cos^2_j^{\text{var}}(k)$, respectively. They are defined by squaring of the factor scores and normalizing
 492 them by Euclidian norm across components:

$$493 \quad \cos^2_i^{\text{phe}}(k) = \frac{(f_{i,k}^p)^2}{\sum_{k'} (f_{i,k'}^p)^2}$$

$$494 \quad \cos^2_j^{\text{var}}(k) = \frac{(f_{j,k}^v)^2}{\sum_{k'} (f_{j,k'}^v)^2}$$

495 By definition, the sum of squared cosine scores across a latent component for a given
 496 phenotype or variant equals to one, i.e. $\sum_k \cos^2_i^{\text{phe}}(k) = \sum_k \cos^2_j^{\text{var}}(k) = 1$. While singular
 497 values in the diagonal matrix S quantify the importance of latent components for the global latent
 498 structure, the phenotype or variant squared cosine score quantifies the relative importance of
 499 each component in the context of a given phenotype or a variant. The squared cosine scores for
 500 the phenotypes highlighted in the study is summarized in Fig. S3 and Supplementary Fig. S9.

501 Note that squared cosine scores and contribution scores are two complementary scoring
 502 metrics to quantify the relationship among phenotypes, components, variants, and genes. It
 503 does not necessarily have inverse mapping property. For example, it is possible to see a
 504 situation, where for a given phenotype p , phenotype squared cosine score identifies k as the top
 505 key component, but phenotype contribution score for k identifies p' ($p' \neq p$) as the top driving
 506 phenotype for the component k . This is because the two scores, contribution score and squared
 507 cosine score, are both defined by normalizing singular vector and principal component vector
 508 matrices, respectively, but with respect to different slices: one for row and the other for column.

509 Genomic region enrichment analysis with GREAT

510 We applied the genomic region enrichment analysis tool (GREAT version 4.0.3) to each DeGAs
511 components²⁰. We used the mouse genome informatics (MGI) phenotype ontology, which
512 contains manually curated knowledge about hierarchical structure of phenotypes and genotype-
513 phenotype mapping of mouse³². We downloaded their ontologies on 2017-09-28 and mapped
514 MGI gene identifiers to Ensembl human gene ID through unambiguous one-to-one homology
515 mapping between human and mouse Ensembl IDs. We removed ontology terms that were
516 labelled as “obsolete”, “bad”, or “unknown” from our analysis. As a result, we obtained 709,451
517 mapping annotation spanning between 9,554 human genes and 9,592 mouse phenotypes.

518 For each DeGAs component, we selected the top 5,000 variants according to their
519 variant contribution score and performed enrichment analysis with the default parameter as
520 described elsewhere²⁰. Since we included the non-coding variants in the analysis, we focused
521 on GREAT binomial genomic region enrichment analysis based on the size of regulatory
522 domain of genes, and quantified the significance of enrichment in terms of binomial fold
523 enrichment and binomial p-value. Given that we have 9,561 terms in the ontology, we set a
524 Bonferroni p-value threshold of 5×10^{-6} . To illustrate the results of the genomic region
525 enrichment analysis for the phenotypes of our interest, we made circular bar plots using the R
526 package ggplot2, where each of the key components are displayed in the innermost track with
527 their phenotype squared cosine score to be proportional to their angle, and the resulted
528 significant ontology terms are represented as the bars. The binomial fold change is represented
529 as the radius and the binomial p-value is represented as color gradient in a log scale in the plot
530 (Fig. 3b, Supplementary Fig. S7-8, Supplementary Table S5-7).

531 Quality control of variant calling with intensity plots

532 To investigate the quality of variant calling for the two PTVs highlighted in the study, we
533 manually inspected intensity plots. These plots are available on Global Biobank Engine.

- 534 • <https://biobankengine.stanford.edu/intensity/rs114285050>
- 535 • <https://biobankengine.stanford.edu/intensity/rs150090666>

536 Phenome-wide association analysis

537 To explore the functional roles of the two PTVs across thousands of potentially correlated
538 phenotypes, we performed a phenome-wide association study (PheWAS). We report the
539 statistically significant ($p < 0.001$) associations with phenotypes with at least 1,000 case count
540 (binary phenotypes) or 1,000 individuals with measurements with non-missing values
541 (quantitative phenotypes) (Fig. 3d, Supplementary Fig. S10). The results of this PheWAS are
542 also available as interactive plots as a part of Global Biobank Engine.

- 543 • <https://biobankengine.stanford.edu/variant/5-145895394>
- 544 • <https://biobankengine.stanford.edu/variant/11-14865399>

545 Univariate regression analysis for the identified PTVs

546 To quantify the effects of the two PTVs on obesity, we performed univariate regression analysis.
547 We extracted individual-level genotype information for the two PTVs with the PLINK2 pgen
548 Python API (<http://www.cog-genomics.org/plink/2.0/>)⁴⁸. After removing individuals with missing
549 values for BMI and genotype, we performed linear regression for BMI
550 (<http://biobank.ctsu.ox.ac.uk/crystal/field.cgi?id=21001>) with age, sex, and the first four genomic
551 PCs as covariates:
552
$$\text{BMI} \sim 0 + \text{age} + \text{as.factor}(\text{sex}) + \text{PC1} + \text{PC2} + \text{PC3} + \text{PC4} + \text{as.factor}(\text{PTV})$$

553 where, PC1-4 denotes the first four components of genomic principal components, PTV ranges
554 in 0, 1, or 2 and it indicates the number of minor alleles that the individuals have.

555 Mouse 3T3-L1 cell culture and differentiation

556 3T3-L1 preadipocytes were cultured in Dulbecco's Modified Eagle's Medium (DMEM) containing
557 10% fetal bovine serum (FBS) and antibiotics (100 U/mL of penicillin G and 100 µg/mL of
558 streptomycin) at 37°C in a humidified atmosphere containing 5% CO₂. To obtain fully
559 differentiated adipocytes, 3T3-L1 preadipocytes were grown into 2-day post-confluence, and
560 then differentiation was induced by using a standard differentiation cocktail containing 0.5 mM of
561 IBMX, 1 µM of dexamethasone, 1 µg/mL of insulin, and 10% FBS. After 48 h, medium was
562 changed into DMEM supplemented with 10% FBS and 1 µg/mL of insulin and replenished every
563 48 h for an additional 6 days.

564 Human SGBS cell culture and differentiation

565 SGBS cells were cultured in DMEM/F12 containing 33 µM biotin, 17 µM pantothenate,
566 0.1 mg/mg streptomycin and 100 U/mL penicillin (0F medium) supplemented with 10% FBS in a
567 5% CO₂ incubator. To initiate differentiation, confluent cells were stimulated by 0F media
568 supplemented with 0.01 mg/mL human transferrin, 0.2 nM T3, 100 nM cortisol, 20 nM insulin,
569 250 µM IBMX, 25 nM dexamethasone and 2 µM rosiglitazone. After day 4, the differentiating
570 cells were kept in 0F media supplemented with 0.01 mg/mL human transferrin, 100 nM cortisol,
571 20 nM insulin and 0.2 nM T3 for additional 8-10 days until cells were fully differentiated.

572 siRNA knockdown in 3T3-L1 preadipocytes

573 At 80% confluence, 3T3-L1 preadipocytes were transfected with 50 nM siRNA against
574 *Gpr151* (Origene #SR412988), *Pde3b* (Origene #SR422062), or scrambled negative control
575 (Origene #SR30004) using Lipofectamine™ RNAiMAX Transfection Reagent (Invitrogen)
576 following the manufacturer's protocol. The transfected cells were incubated for 48 h and then
577 subjected to differentiation.

578 Reverse transcription (RT) and qPCR analysis

579 Total RNA was extracted using TRIzol reagent (Invitrogen), following the manufacturer's
580 instruction. RNA was converted to cDNA using High-Capacity cDNA Reverse Transcription Kit
581 (Applied Biosystems). Quantitative PCR reactions were prepared with TaqMan™ Fast
582 Advanced Master Mix (Thermo Fisher Scientific) and performed on ViiA 7 Real-Time PCR
583 System (Thermo Fisher Scientific). All data were normalized to the content of Cyclophilin A
584 (PPIA), as the endogenous control. TaqMan primer information for RT-qPCR is listed below:
585 *GPR151* (Hs00972208_s1), *Gpr151* (Mm00808987_s1), *PDE3B* (Hs00265322_m1), *Pde3b*
586 (Mm00691635_m1), *Pparg* (Mm00440940_m1), *Cebpa* (Mm00514283_s1), *Fabp4*
587 (Mm00445878_m1), *PPIA* (Hs04194521_s1), *Ppia* (Mm02342430_g1).

588 Oil Red O staining and quantification

589 Cells were washed twice with PBS and fixed with 10% formalin for 1 h at room temperature.
590 Cells were then washed with 60% isopropanol and stained for 15 min with a filtered Oil Red O
591 solution (mix six parts of 0.35% Oil Red O in isopropanol with four parts of water). After washing
592 with PBS 4 times, cells were maintained in PBS and visualized by inverted microscope. After
593 taking pictures, Oil Red O stain was extracted with 100% isopropanol and the absorbance was
594 measured at 492 nm by a multi-well spectrophotometer (Bio-Rad).

595 Lipolysis assay

596 Glycerol release into the culture medium was used as an index of lipolysis. Fully differentiated
597 3T3-L1 adipocytes were serum starved overnight and then treated with either vehicle (DMSO)
598 or the lipolytic stimuli isoproterenol (ISO, 10 μ M) for 3 h. The culture medium was collected and
599 the glycerol content in the culture medium was measured using an adipocyte lipolysis assay kit
600 (ZenBio #LIP-1-NCL1). Glycerol release into the culture medium was normalized to the protein
601 content of the cells from the same plate.

602 Overexpression of *GPR151* in 3T3-L1 preadipocytes

603 The *GPR151* construct was obtained from Addgene (#66327). This construct includes a
604 cleavable HA signal to promote membrane localization, a FLAG epitope sequence for cell
605 surface staining followed by codon-optimized human *GPR151* sequence⁵³. We PCR-amplified
606 the above sequence with stop codon and assembled it into a lentiviral plasmid (Addgene
607 #85969) with either EF1 α promoter (Addgene # 11154) or aP2 promoter (Addgene # 11424).
608 EF1 α -*GPR151* or aP2-*GPR151* lentiviral plasmid were transfected into human embryonic
609 kidney 293T cells, together with the viral packaging vectors pCMV-dR8.91 and pMD2-G. 72 h
610 after transfection, virus-containing medium was collected, filtered through a 0.45- μ m pore-size
611 syringe filter, and frozen at -80°C. 3T3-L1 preadipocytes at 50% confluence were infected with
612 the lentivirus stocks containing 8 μ g/mL polybrene. Two days after transduction, lentivirus-
613 infected 3T3-L1 preadipocytes were subject to differentiation.

614 Flow cytometry analysis

615 Day 6 differentiating 3T3-L1 adipocytes were collected and washed with ice cold FACS buffer
616 (PBS containing 2% BSA). Cells were first resuspended into FACS staining buffer (BioLegend #
617 420201) at ~1M cells/100 μ l and incubated with anti-mouse CD16/CD32 Fc Block (BioLegend #
618 101319) at room temperature for 10-15 min. Cells were then incubated with APC-conjugated
619 FLAG antibody (BioLegend # 637307) for 20-30 min at room temperature in the dark. Following
620 washing and centrifugation, cells were resuspended in FACS buffer and sorted using a BD
621 InfluxTM Cell Sorter. Cells without FLAG antibody staining were used to determine background
622 fluorescence levels. Cells were sorted based on APC fluorescence and collected directly into
623 TRIzol reagent for RNA extraction.

624 Western Blot Analysis

625 Lysate aliquots containing 50 μ g of proteins were denatured, separated on a 4-10% SDS-
626 polyacrylamide gel, and transferred to nitrocellulose membranes using a Trans-Blot[®] SD Semi-
627 Dry Transfer Cell (Bio-Rad). Membranes were blocked in 5% non-fat milk and incubated
628 overnight at 4 °C with primary antibodies: anti-GPR151 (LSBio # LS-B6760-50) or anti-beta-
629 actin (Cell Signaling #3700). Subsequently, the membranes were incubated for 1 h at room
630 temperature with IRDye[®] 800CW goat-anti-mouse antibody (LI-COR #926-32210). Target
631 proteins were visualized using Odyssey[®] Fc Imaging System (LI-COR).

632 Statistical analysis of functional data

633 Data are expressed as mean \pm SEM. Student's t test was used for single variables, and one-
634 way ANOVA with Bonferroni post hoc correction was used for multiple comparisons using
635 GraphPad Prism 7 software.

636 Acknowledgements

637 This research has been conducted using the UK Biobank Resource under Application Number
638 24983. We thank all the participants in the UK Biobank study. Y.T. is supported by Funai
639 Overseas Scholarship from Funai Foundation for Information Technology and the Stanford
640 University School of Medicine. J.M.J. was funded by grant NNF17OC0025806 from the Novo
641 Nordisk Foundation and the Stanford Bio-X Program. M.A.R. and C.D. are supported by
642 Stanford University and a National Institute of Health center for Multi- and Trans-ethnic Mapping
643 of Mendelian and Complex Diseases grant (5U01 HG009080). C.D. is supported by a
644 postdoctoral fellowship from the Stanford Center for Computational, Evolutionary, and Human
645 Genomics and the Stanford ChEM-H Institute. The primary and processed data used to
646 generate the analyses presented here are available in the UK Biobank access management
647 system (<https://amsportal.ukbiobank.ac.uk/>) for application 24983, "Generating effective
648 therapeutic hypotheses from genomic and hospital linkage data"
649 (<http://www.ukbiobank.ac.uk/wp-content/uploads/2017/06/24983-Dr-Manuel-Rivas.pdf>), and the

650 results are displayed in the Global Biobank Engine (<https://biobankengine.stanford.edu>). We
651 obtained clip-arts for Fig. 1b from Irasutoya (<https://www.irasutoya.com/>) by following their terms
652 and conditions. The copyright of the original clip-arts belongs to Mr. Takashi Mifune. We would
653 like to thank the Customer Solutions Team from Paradigm4 who helped us implement efficient
654 databases for queries and application of inference methods to the data, and also implemented
655 optimized versions of truncated singular value decomposition.

656

657 **Funding:**

658 This work was supported by National Human Genome Research Institute (NHGRI) and National
659 Institute of Diabetes and Digestive and Kidney Diseases (NIDDK) of the National Institutes of
660 Health (NIH) under awards R01HG010140 and R01DK106236. The content is solely the
661 responsibility of the authors and does not necessarily represent the official views of the National
662 Institutes of Health.

663 Author information

664 **Author contributions**

665 M.A.R. and E.I. conceived and designed the study. Y.T. and M.A.R. carried out the statistical
666 and computational analyses with advice from J.M.J., H.H., M.A., C.D., B.N., K.L., T.H., G.B., and
667 E.I. J.L., C.Y.P., and E.I. carried out the functional experiments. Y.T., M.A., and C.D. carried out
668 quality control of the data. C.C. optimized and implemented computational methods. Y.T. and
669 M.A.R. developed the DeGAs app in Global Biobank Engine. M.A.R. supervised computational
670 and statistical aspects of the study. E.I. supervised experimental aspects of the study. The
671 manuscript was written by Y.T., J.L., J.M.J., E.I., and M.A.R.; and revised by all the co-authors.
672 All co-authors have approved of the final version of the manuscript.

673

674 **Competing financial interests**

675 None.

676

677 **Data availability:**

678 Data is displayed in the Global Biobank Engine (<https://biobankengine.stanford.edu>).

679 References

- 680 1. Welter, D. *et al.* The NHGRI GWAS Catalog, a curated resource of SNP-trait associations.
681 *Nucleic Acids Res.* **42**, 1001–1006 (2014).
- 682 2. Visscher, P. M. *et al.* 10 Years of GWAS Discovery: Biology, Function, and Translation. *Am.*
683 *J. Hum. Genet.* **101**, 5–22 (2017).

- 684 3. The International Schizophrenia Consortium. Common polygenic variation contributes to risk
685 of schizophrenia and bipolar disorder. *Nature* **460**, 748–752 (2009).
- 686 4. Purcell, S. M. *et al.* A polygenic burden of rare disruptive mutations in schizophrenia. *Nature*
687 **506**, 185–190 (2014).
- 688 5. Boyle, E. A., Li, Y. I. & Pritchard, J. K. An Expanded View of Complex Traits: From
689 Polygenic to Omnigenic. *Cell* **169**, 1177–1186 (2017).
- 690 6. Plenge, R. M., Scolnick, E. M. & Altshuler, D. Validating therapeutic targets through human
691 genetics. *Nat. Rev. Drug Discov.* **12**, 581–594 (2013).
- 692 7. Waring, R. Sequence Variations in PCSK9, Low LDL, and Protection against Coronary
693 Heart Disease. *N Engl J Med* **9** (2006).
- 694 8. Cohen, J. *et al.* Low LDL cholesterol in individuals of African descent resulting from frequent
695 nonsense mutations in PCSK9. *Nat. Genet.* **37**, 161–165 (2005).
- 696 9. Rivas, M. A. *et al.* Deep resequencing of GWAS loci identifies independent rare variants
697 associated with inflammatory bowel disease. *Nat. Genet.* **43**, 1066–1073 (2011).
- 698 10. Rivas, M. A. *et al.* A protein-truncating R179X variant in RNF186 confers protection against
699 ulcerative colitis. *Nat. Commun.* **7**, 12342 (2016).
- 700 11. Nejentsev, S., Walker, N., Riches, D., Egholm, M. & Todd, J. A. Rare Variants of IFIH1, a
701 Gene Implicated in Antiviral Responses, Protect Against Type 1 Diabetes. *Science* **324**,
702 387–389 (2009).
- 703 12. DeBoever, C. *et al.* Medical relevance of protein-truncating variants across 337,205
704 individuals in the UK Biobank study. *Nat. Commun.* **9**, 1612 (2018).
- 705 13. Tipney, H. *et al.* The support of human genetic evidence for approved drug indications. *Nat.*
706 *Genet.* **47**, 1–7 (2015).
- 707 14. Bycroft, C. *et al.* The UK Biobank resource with deep phenotyping and genomic data.
708 *Nature* **562**, 203–209 (2018).

- 709 15. Stewart, G. On the Early History of the Singular Value Decomposition. *SIAM Rev.* **35**, 551–
710 566 (1993).
- 711 16. Novembre, J. *et al.* Genes mirror geography within Europe. *Nature* **456**, 98–101 (2008).
- 712 17. Varah, J. M. On the Numerical Solution of Ill-Conditioned Linear Systems with Applications
713 to Ill-Posed Problems. *SIAM J. Numer. Anal.* **10**, 257–267 (1973).
- 714 18. Hanson, R. J. A Numerical Method for Solving Fredholm Integral Equations of the First Kind
715 Using Singular Values. *SIAM J. Numer. Anal.* **8**, 616–622 (1971).
- 716 19. Hansen, P. C. The truncatedSVD as a method for regularization. *BIT Numer. Math.* **27**,
717 534–553 (1987).
- 718 20. McLean, C. Y. *et al.* GREAT improves functional interpretation of cis-regulatory regions.
719 *Nat. Biotechnol.* **28**, 495–501 (2010).
- 720 21. Rivas, M. A. *et al.* Effect of predicted protein-truncating genetic variants on the human
721 transcriptome. *Science* **348**, 666–669 (2015).
- 722 22. MacArthur, D. G. *et al.* A Systematic Survey of Loss-of-Function Variants in Human Protein-
723 Coding Genes. *Science* **335**, 823–828 (2012).
- 724 23. Abdi, H. & Williams, L. J. Principal component analysis. *Wiley Interdiscip. Rev. Comput.*
725 *Stat.* **2**, 433–459 (2010).
- 726 24. Bigaard, J. *et al.* Body Fat and Fat-Free Mass and All-Cause Mortality. *Obes. Res.* **12**,
727 1042–1049 (2004).
- 728 25. Foster, K. R. & Lukaski, H. C. Whole-body impedance--what does it measure? *Am. J. Clin.*
729 *Nutr.* **64**, 388S-396S (1996).
- 730 26. Talma, H. *et al.* Bioelectrical impedance analysis to estimate body composition in children
731 and adolescents: a systematic review and evidence appraisal of validity, responsiveness,
732 reliability and measurement error. *Obes. Rev. Off. J. Int. Assoc. Study Obes.* **14**, 895–905
733 (2013).

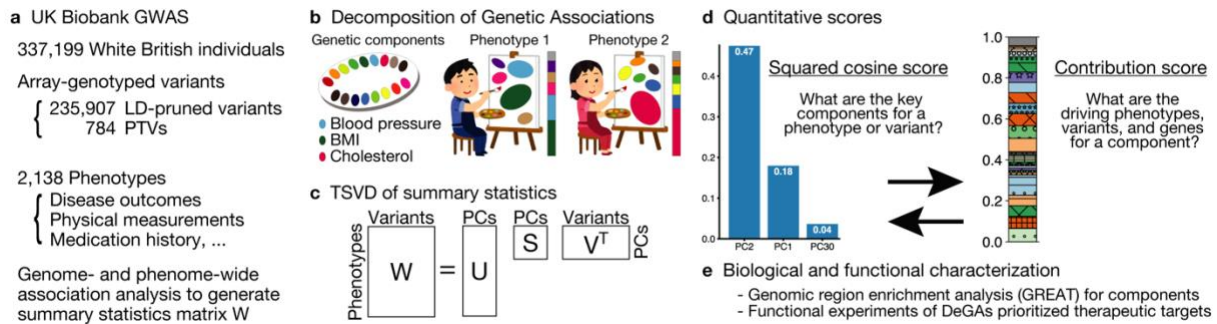
- 734 27. Moran, A. E. *et al.* The Global Burden of Ischemic Heart Disease in 1990 and 2010.
735 *Circulation* (2014).
- 736 28. Lammert, F. *et al.* Gallstones. *Nat. Rev. Dis. Primer* **2**, 16024 (2016).
- 737 29. Zhou, D., Wu, J. & Luo, G. Body mass index and risk of non-melanoma skin cancer:
738 cumulative evidence from prospective studies. *Sci. Rep.* **6**, 37691 (2016).
- 739 30. Khera, A. V. & Kathiresan, S. Is Coronary Atherosclerosis One Disease or Many?: Setting
740 Realistic Expectations for Precision Medicine. *Circulation* **135**, 1005–1007 (2017).
- 741 31. Bennion, L. J. & Grundy, S. M. Risk Factors for the Development of Cholelithiasis in Man. *N.*
742 *Engl. J. Med.* **299**, 1161–1167 (1978).
- 743 32. Smith, C. L. & Eppig, J. T. Expanding the mammalian phenotype ontology to support
744 automated exchange of high throughput mouse phenotyping data generated by large-scale
745 mouse knockout screens. *J. Biomed. Semant.* **6**, 11 (2015).
- 746 33. Krawczyk, M. *et al.* Phytosterol and cholesterol precursor levels indicate increased
747 cholesterol excretion and biosynthesis in gallstone disease. *Hepatology* **55**, 1507–1517
748 (2012).
- 749 34. Abul-Husn, N. S. *et al.* A Protein-Truncating HSD17B13 Variant and Protection from Chronic
750 Liver Disease. *N. Engl. J. Med.* **378**, 1096–1106 (2018).
- 751 35. Green, H. & Kehinde, O. An established preadipose cell line and its differentiation in culture
752 II. Factors affecting the adipose conversion. *Cell* **5**, 19–27 (1975).
- 753 36. Wabitsch, M. *et al.* Characterization of a human preadipocyte cell strain with high capacity
754 for adipose differentiation. *Int. J. Obes.* **25**, 8–15 (2001).
- 755 37. Broms, J. *et al.* Monosynaptic retrograde tracing of neurons expressing the G-protein
756 coupled receptor Gpr151 in the mouse brain. *J. Comp. Neurol.* **525**, 3227–3250 (2017).
- 757 38. Shakur, Y. *et al.* Regulation and function of the cyclic nucleotide phosphodiesterase (PDE3)
758 gene family. in *Progress in Nucleic Acid Research and Molecular Biology* **66**, 241–277
759 (Elsevier, 2000).

- 760 39. Chung, Y. W. *et al.* White to beige conversion in PDE3B KO adipose tissue through
761 activation of AMPK signaling and mitochondrial function. *Sci. Rep.* **7**, 40445 (2017).
- 762 40. Chung, Y. W. *et al.* Targeted disruption of PDE3B, but not PDE3A, protects murine heart
763 from ischemia/reperfusion injury. *Proc. Natl. Acad. Sci.* 201416230 (2015).
764 doi:10.1073/pnas.1416230112
- 765 41. Emdin, C. A. *et al.* Genetic Association of Waist-to-Hip Ratio With Cardiometabolic Traits,
766 Type 2 Diabetes, and Coronary Heart Disease. *JAMA* **317**, 626–634 (2017).
- 767 42. Collins, F. S. & Varmus, H. A New Initiative on Precision Medicine. *N. Engl. J. Med.* **372**,
768 793–795 (2015).
- 769 43. Chen, Z. *et al.* China Kadoorie Biobank of 0.5 million people: survey methods, baseline
770 characteristics and long-term follow-up. *Int. J. Epidemiol.* **40**, 1652–1666 (2011).
- 771 44. Christensen, H., Nielsen, J. S., Sorensen, K. M., Melbye & Brandslund, I. New national
772 Biobank of The Danish Center for Strategic Research on Type 2 Diabetes (DD2). *Clin.*
773 *Epidemiol.* **37** (2012). doi:10.2147/CLEP.S33042
- 774 45. Avlund, K. *et al.* Copenhagen Aging and Midlife Biobank (CAMB): An Introduction. *J. Aging*
775 *Health* **26**, 5–20 (2014).
- 776 46. Emdin, C. A. *et al.* Analysis of predicted loss-of-function variants in UK Biobank identifies
777 variants protective for disease. *Nat. Commun.* **9**, 1613 (2018).
- 778 47. McInnes, G. *et al.* Global Biobank Engine: enabling genotype-phenotype browsing for
779 biobank summary statistics. *bioRxiv* 304188 (2018). doi:10.1101/304188
- 780 48. Chang, C. C. *et al.* Second-generation PLINK: rising to the challenge of larger and richer
781 datasets. *GigaScience* **4**, 7 (2015).
- 782 49. Baglama, J. & Reichel, L. Augmented Implicitly Restarted Lanczos Bidiagonalization
783 Methods. *SIAM J. Sci. Comput.* **27**, 19–42 (2005).

- 784 50. Brown, P. G. Overview of sciDB: large scale array storage, processing and analysis. in
785 *Proceedings of the 2010 international conference on Management of data - SIGMOD '10*
786 963 (ACM Press, 2010). doi:10.1145/1807167.1807271
- 787 51. Gower, J., Lubbe, S. & Roux, N. le. *Understanding Biplots*. (John Wiley & Sons, Ltd, 2011).
788 doi:10.1002/9780470973196
- 789 52. Gabriel, K. R. The Biplot Graphic Display of Matrices with Application to Principal
790 Component Analysis. *Biometrika* **58**, 453 (1971).
- 791 53. Kroeze, W. K. *et al.* PRESTO-Tango as an open-source resource for interrogation of the
792 druggable human GPCRome. *Nat. Struct. Mol. Biol.* **22**, 362–369 (2015).
793

794 **Figures**

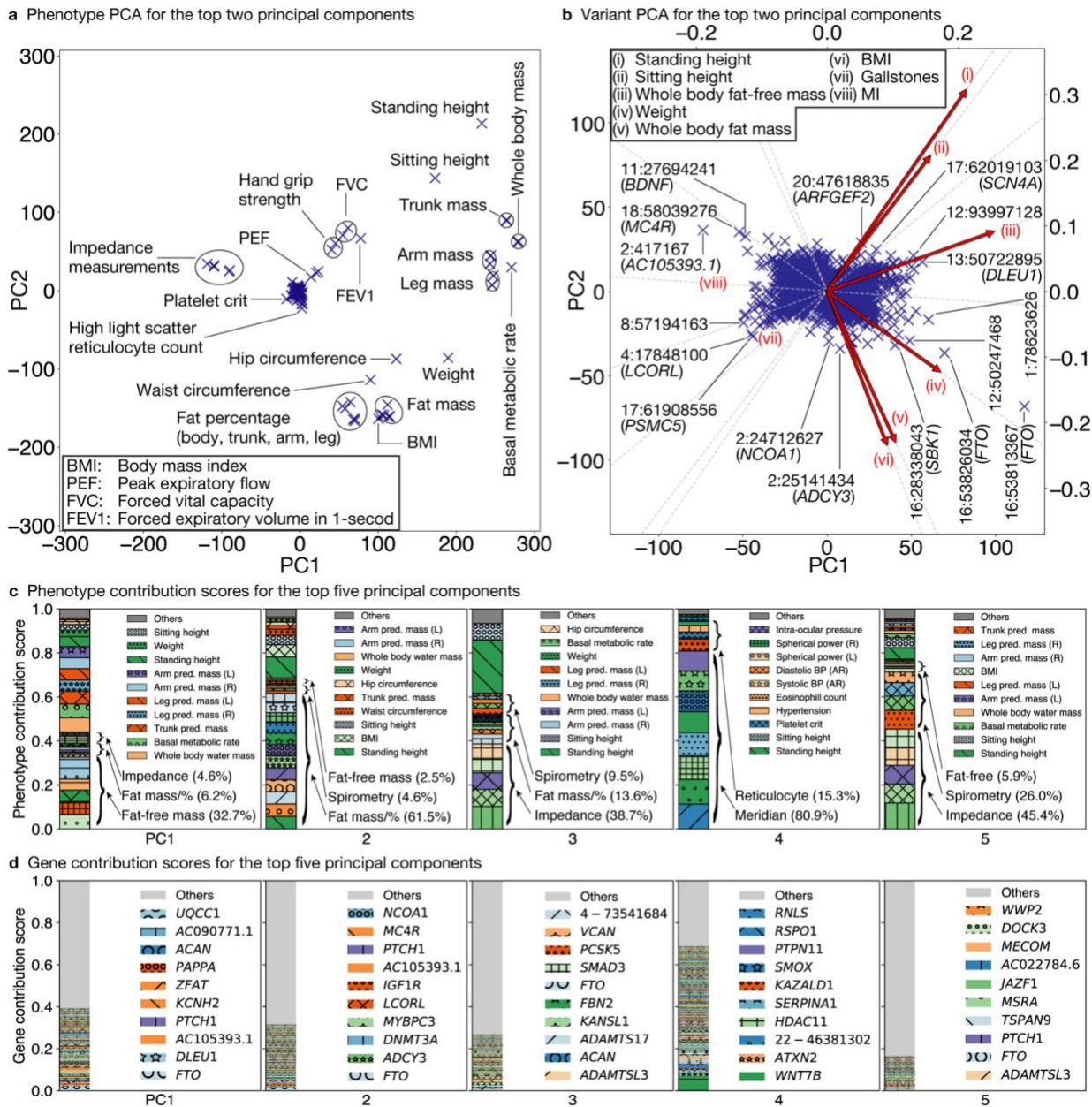
795 **Figure 1**



796
 797
 798
 799
 800
 801
 802
 803
 804
 805
 806
 807
 808
 809

Fig.1 Illustrative study overview. **a** Summary of the UK Biobank genotype and phenotype data used in the study. We included White British individuals and analyzed LD-pruned and quality-controlled variants in relation to 2,138 phenotypes with a minimum of 100 individuals as cases (binary phenotypes) or non-missing values (quantitative phenotypes) (Supplementary Table S1-2). **b** Decomposition of Genetic Associations (DeGAs) characterizes latent genetic components, which are represented as different colors on the palette, with an unsupervised learning approach – truncated singular value decomposition (TSVD), followed by identification of the key components for each phenotype of our interest (painting phenotypes with colors) and annotation of each of the components with driving phenotypes, variants, and genes (finding the meanings of colors). **c** TSVD applied to decompose genome- and phenome-wide summary statistic matrix W to characterize latent components. U , S , and V represent resulting matrices of singular values and vectors. **d** We used the squared cosine score and the contribution score, to quantify compositions and biomedical relevance of latent components. **e** We applied the genomic region enrichment analysis tool (GREAT) for biological characterization of each component and performed functional experiments focusing on adipocyte biology.

810 Figure 2

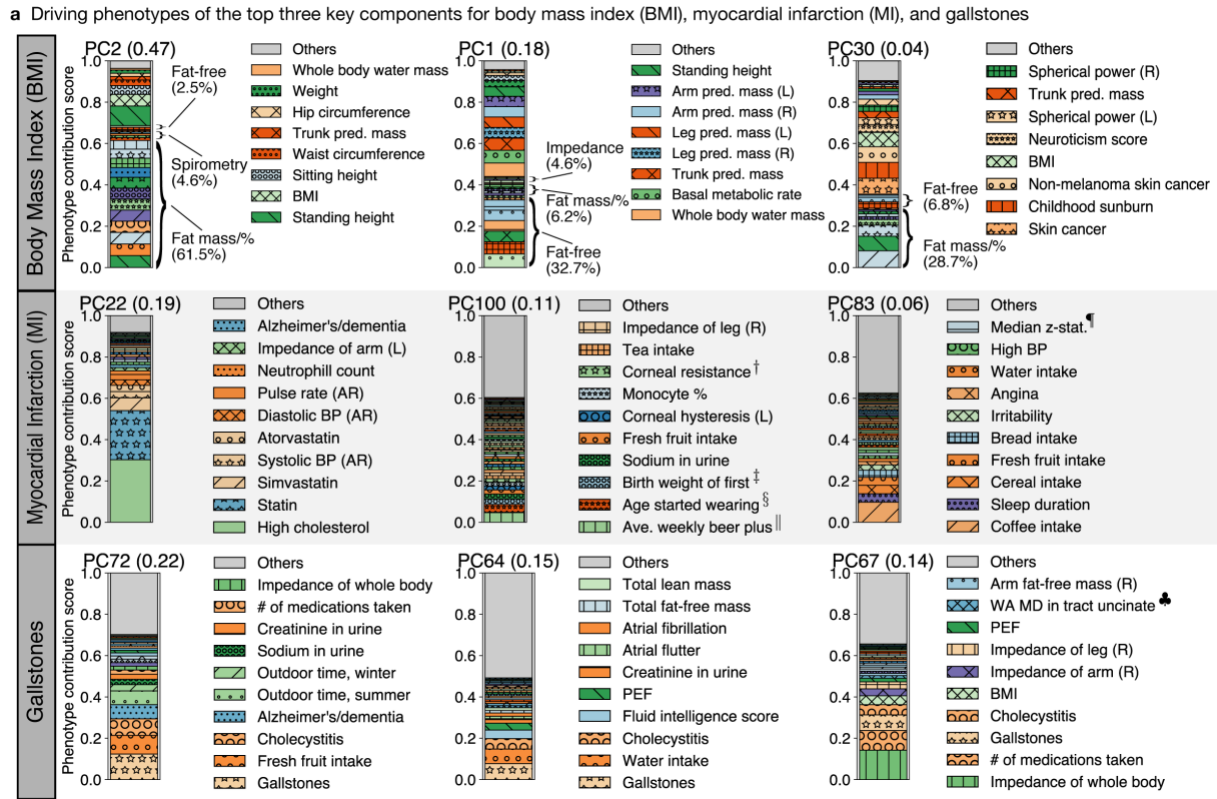


811
812
813
814
815
816
817
818
819
820
821
822
823
824

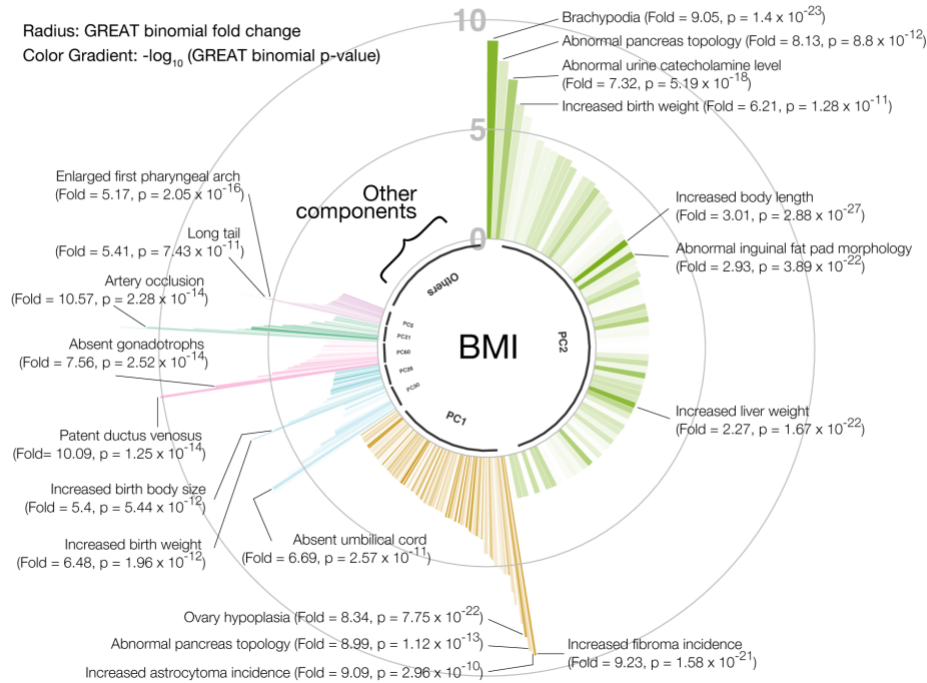
Fig. 2 Characterization of latent structures of genetic associations from genome- and-phenome-wide association summary statistics with DeGAs. **a-b** Components from truncated singular value decomposition (TSVD) corresponds to principal components in the phenotype (**a**) and variant (**b**) spaces. The first two components of all variants, excluding the MHC region, and relevant phenotypes are shown. **b** For variant PCA, we show biplot arrows (red) for selected phenotypes to help interpretation of the direction of principal components (Methods). The variants are labeled based on the genomic positions and the corresponding gene symbols. For example, "16:53813367 (*FTO*)" indicates the variant in gene *FTO* at position 53813367 on chromosome 16. **c-d** Phenotype (**c**) and gene (**d**) contribution scores for the first five components. PC1 is driven by largest part of the body mass that accounts for the "healthy part" (main text) including whole-body fat-free mass and genetic variants on *FTO* and *DLEU1*, whereas PC2 is driven by fat-related measurements, PC3 is driven by bioelectrical impedance measurements, PC4 is driven by eye measurements, and PC5 is driven by bioelectrical impedance and spirometry measurements along with the corresponding genetic variants (main text, Supplementary Table S3-4). Each colored segment represents a phenotype or gene with at least 0.5% and 0.05% of phenotype and gene contribution scores, respectively, and the rest is aggregated as others on the top of the stacked bar plots. The major

825 contributing phenotype groups (Methods, Supplementary Table S3) and additional top 10 phenotypes and the top 10 genes for each
826 component are annotated in **c** and **d**, respectively. Abbreviations. pred.: predicted, %: percentage, mass/% mass and percentage,
827 BP: blood pressure, AR: automated reading, L: left, R: right.

828 Figure 3



b Ontology enrichment analysis with the genomic region enrichment analysis tool (GREAT) for body mass index

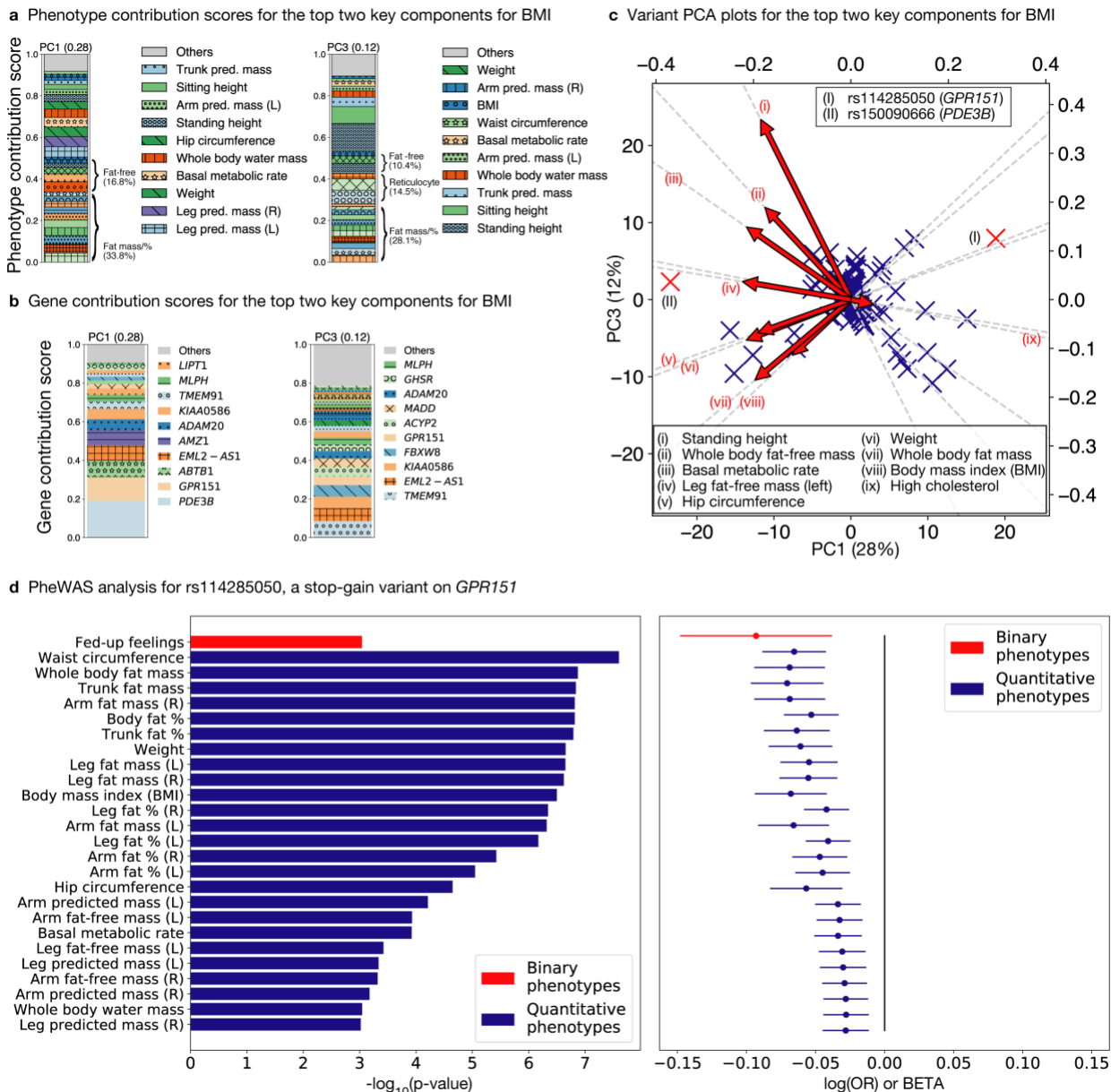


829
830
831
832

Fig.3 The top three key latent components from DeGAs of coding and non-coding variants for body mass index (BMI), myocardial infarction (MI), and gallstones. **a** The top three key components for each phenotype are identified by phenotype squared cosine scores and characterized with the driving phenotypes by phenotype contribution scores (Methods). Each colored segment

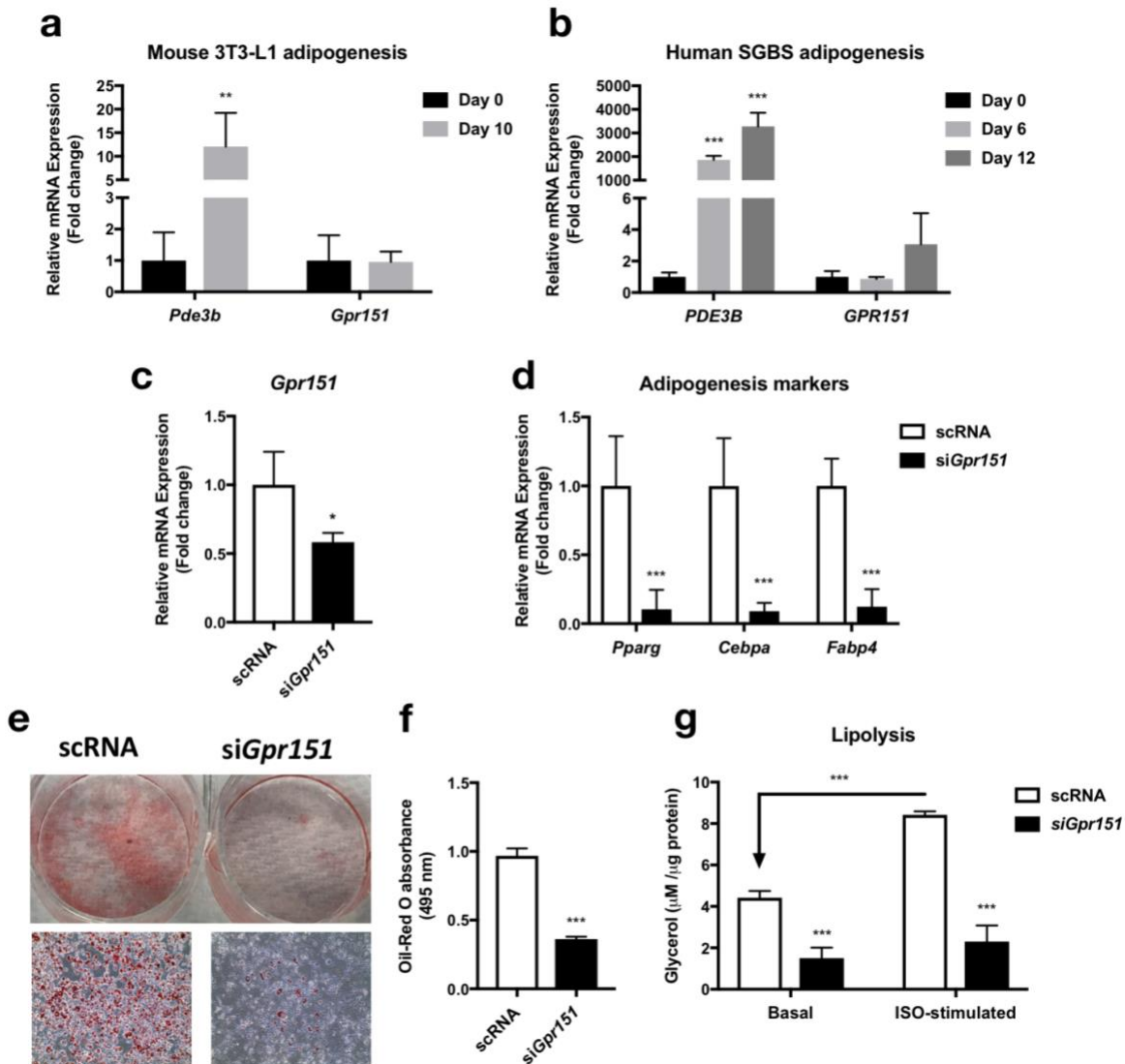
833 represents a phenotype with at least 0.5% of phenotype contribution scores for each of the component and the rest of the
834 phenotypes are aggregated as others and shown as the gray bar on the top. For BMI, additional phenotype grouping is applied
835 (Methods, Supplementary Table S3). **b** Biological characterization of driving non-coding and coding variants of the key components
836 for BMI with GREAT. The key components are shown proportional to their squared cosine score along with significantly enriched
837 terms in mouse MGI phenotype ontology. The radius represents binomial fold change and the color gradient represents p-value
838 from GREAT ontology enrichment analysis. Abbreviations. pred.: predicted, #: number, %: percentage, mass/% mass and
839 percentage, BP: blood pressure, AR: automated reading, L: left, R: right, WA: weighted average. †: Corneal resistance factor (right),
840 ‡: Birth weight of first child, §: Age started wearing glasses or contact lenses, ||: Average weekly beer plus cider intake, ¶: Median z-
841 statistic (in group-defined mask) for shapes activation, ♣: Weighted-mean MD in tract uncinata fasciculus (right).

842 **Figure 4**



843 **Fig. 4** DeGAs applied to the protein-truncating variants (PTVs) dataset. **a-b** Phenotype (**a**) and gene (**b**) contribution scores for the
 844 top key components associated with BMI based on phenotype grouping (Methods, Supplementary Table S3). **c** Variant PCA plot
 845 with biplot annotations for the top two components (Methods). The identified targets for functional follow-up (main text) are marked
 846 as (I) rs114285050 (a stop-gain variant on *GPR151*) and (II) rs150090666 (*PDE3B*). **d** Phenome-wide association analysis for
 847 *GPR151* rs114285050. The p-values (left) and log odds ratio (OR) (binary phenotypes, shown as red) or beta (quantitative
 848 phenotypes, shown as blue) (right) along with 95% confidence interval are shown for the phenotypes with minimum case count of
 849 1,000 (binary phenotypes) or 1,000 individuals with non-missing values (quantitative phenotypes) and strong association ($p < 0.001$)
 850 and with this variants among all the phenotypes used in the study. Abbreviations: L: left, R: right, %: percentage, pred: predicted.
 851

852 Figure 5



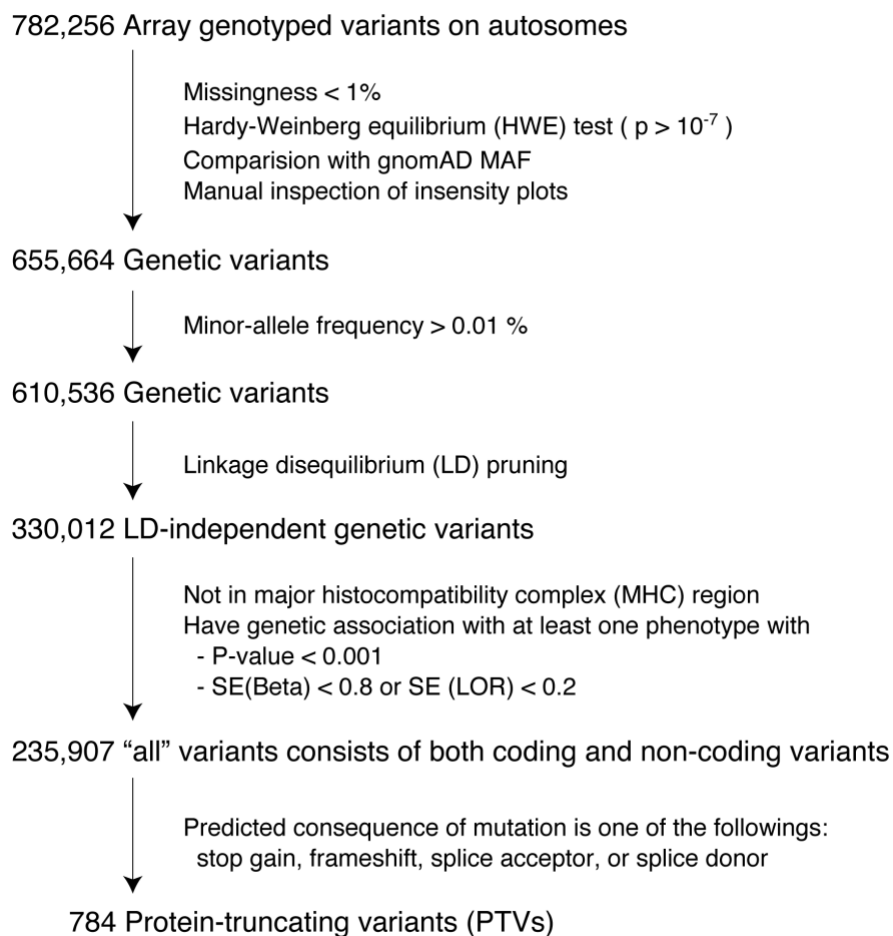
853
854 **Fig. 5** Experimental validation of *GPR151* and *PDE3B* function in cellular models of adipogenesis. **a-b** qPCR analysis of gene
855 expression patterns of *PDE3B* and *GPR151* during **(a)** mouse 3T3-L1 adipogenesis and **(b)** human SGBS adipogenesis. **c** qPCR
856 analysis of *Gpr151* mRNA knockdown in 3T3-L1 preadipocytes. **d** qPCR analysis of the effect of siGpr151 knockdown on
857 adipogenesis markers, *Pparg*, *Cebpa* and *Fabp4*. **e-g** Oil-Red O staining (**e**), quantification of lipid droplets (**f**), and lipolysis (**g**) in
858 scRNA- or siGpr151-transfected adipocytes. Means \pm SEM are shown (**p-value<0.01, ***p-value<0.001, *p-value <0.05). scRNA:
859 scrambled siRNA. ISO: isoproterenol.

860 Supplementary Materials

861 List of supplementary materials

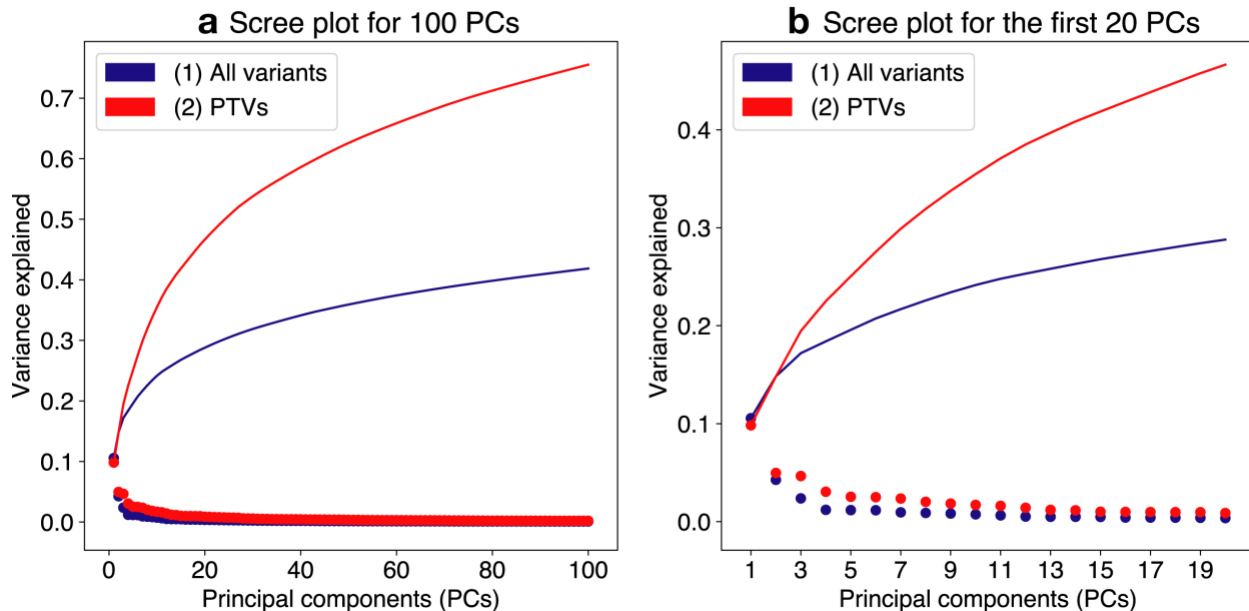
- 862 ● Fig. S1: Variant filtering workflow
- 863 ● Fig. S2: Scree plot
- 864 ● Fig. S3: Squared cosine score (all variants dataset)
- 865 ● Fig. S4: Gene contribution score (all variants dataset)
- 866 ● Fig. S5: Variant PCA plot for MI
- 867 ● Fig. S6: Variant PCA plot for gallstones
- 868 ● Fig. S7: GREAT enrichment analysis for MI
- 869 ● Fig. S8: GREAT enrichment analysis for gallstones
- 870 ● Fig. S9: Squared cosine score of BMI (PTVs dataset)
- 871 ● Fig. S10: PheWAS analysis for *PDB3B*
- 872 ● Fig. S11: Univariate regression analysis for *GPR151*
- 873 ● Fig. S12: Univariate regression analysis for *PDE3B*
- 874 ● Fig. S13: *GPR151* overexpression
- 875 ● Fig. S14: Effects of *Pde3b* knockdown in 3T3-L1 adipogenesis
- 876 ● Table S1: List of phenotype categories
- 877 ● Table S2: List of phenotypes
- 878 ● Table S3: Phenotype groupings for visualization
- 879 ● Table S4: Summary of contribution scores for the key components
- 880 ● Table S5: GREAT enrichment analysis for BMI
- 881 ● Table S6: GREAT enrichment analysis for MI
- 882 ● Table S7: GREAT enrichment analysis for gallstones
- 883 ● Table S8: PheWAS analysis for rs114285050 (*GPR151*)
- 884 ● Table S9: PheWAS analysis for rs150090666 (*PDE3B*)

885 **Fig. S1: Variant filtering workflow**



886
887 **Fig. S1** Illustrative summary of the variant filters used in the study. The last two variant sets
888 ("all" variants and PTVs) are used in the study. Abbreviations. SE: standard error. LOR: log
889 odds ratio.

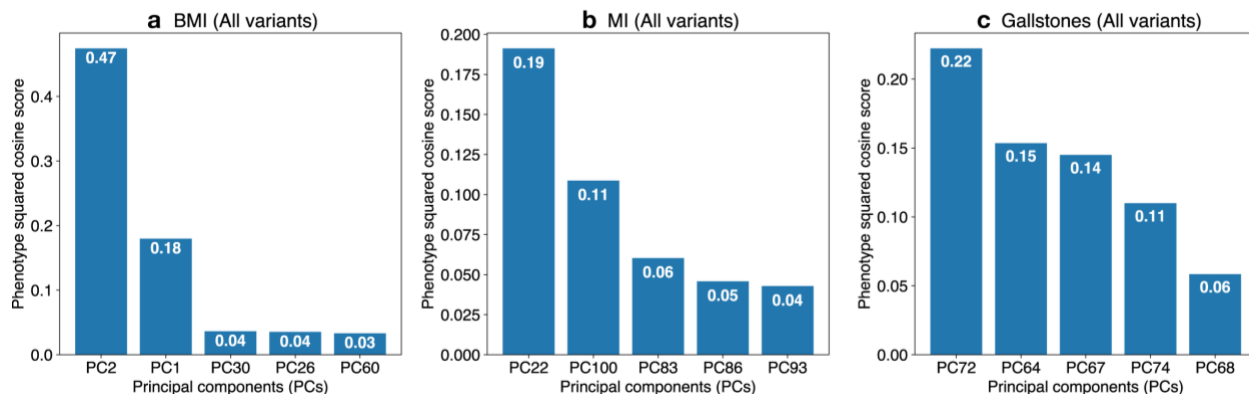
890 Fig. S2: Scree plot



891
892

893 **Fig. S2** Scree plot summarizes variance explained in each of the top 100 (a) and 20 (b)
894 components. The scree plots are shown for two datasets consists of LD-pruned and QC-filtered
895 sets of array-genotyped variants outside of MHC region: (1) all array-genotyped variants, which
896 includes coding and non-coding variants (blue) and (2) protein-truncating variants (PTVs, red).
897 For each component, we calculate the variance explained defined as squared eigenvalues
898 divided by the total variance in the original matrix (Methods). We plotted those values
899 and cumulative values as lines.

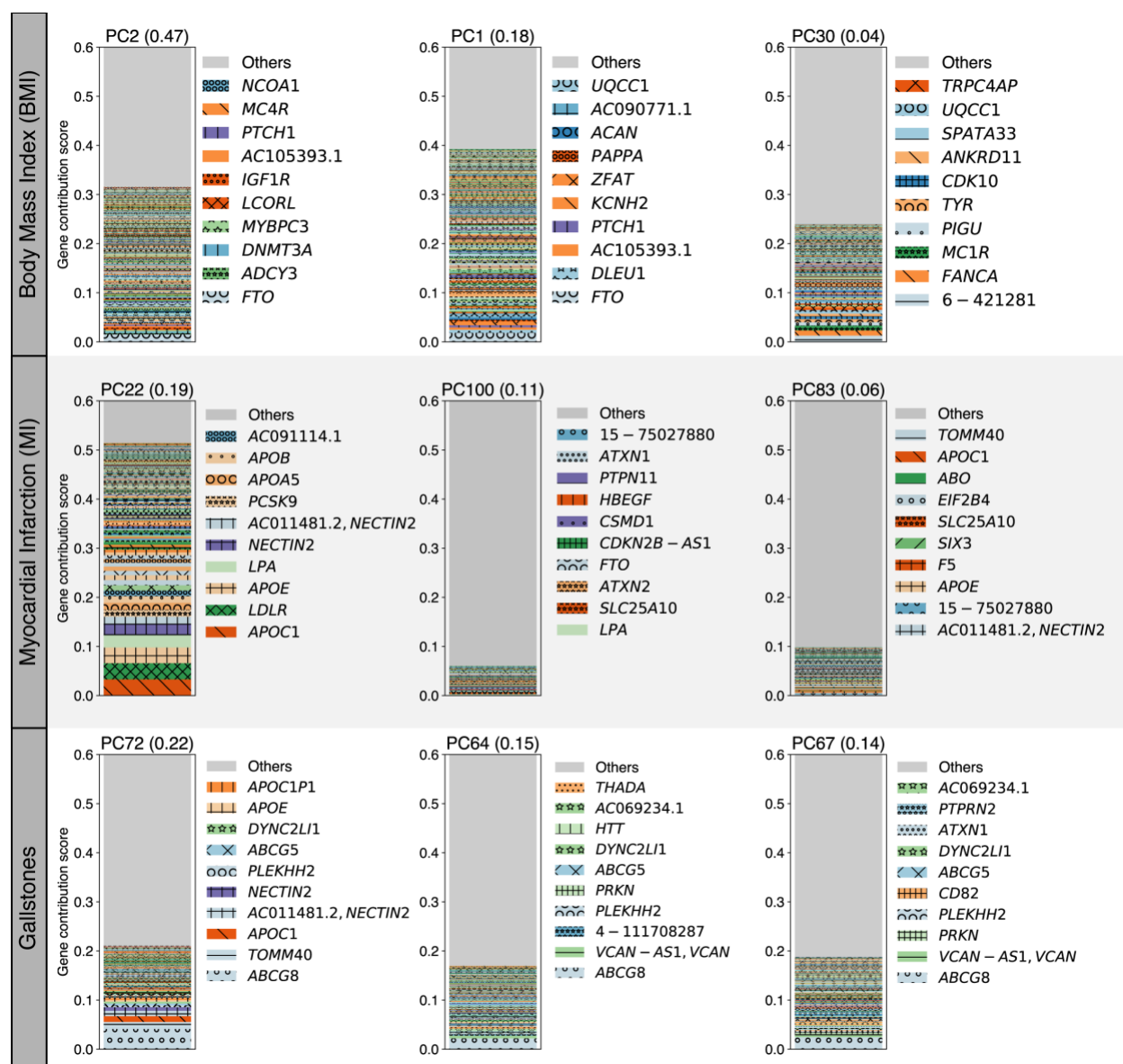
900 Fig. S3: Squared cosine score (all variants dataset)



901
902

903 **Fig. S3** Identification of the key components with phenotype squared cosine scores. Squared
904 cosine score quantifies relative importance of the key components for a given phenotype. The
905 top five key components are identified for all variant dataset that includes both coding and non-
906 coding variants for three phenotypes: **a** body mass index (BMI), **b** myocardial infarction (MI),
907 and **c** gallstones. The top five key components are shown on the horizontal axis and the
908 corresponding squared cosine scores are shown on the vertical axis.

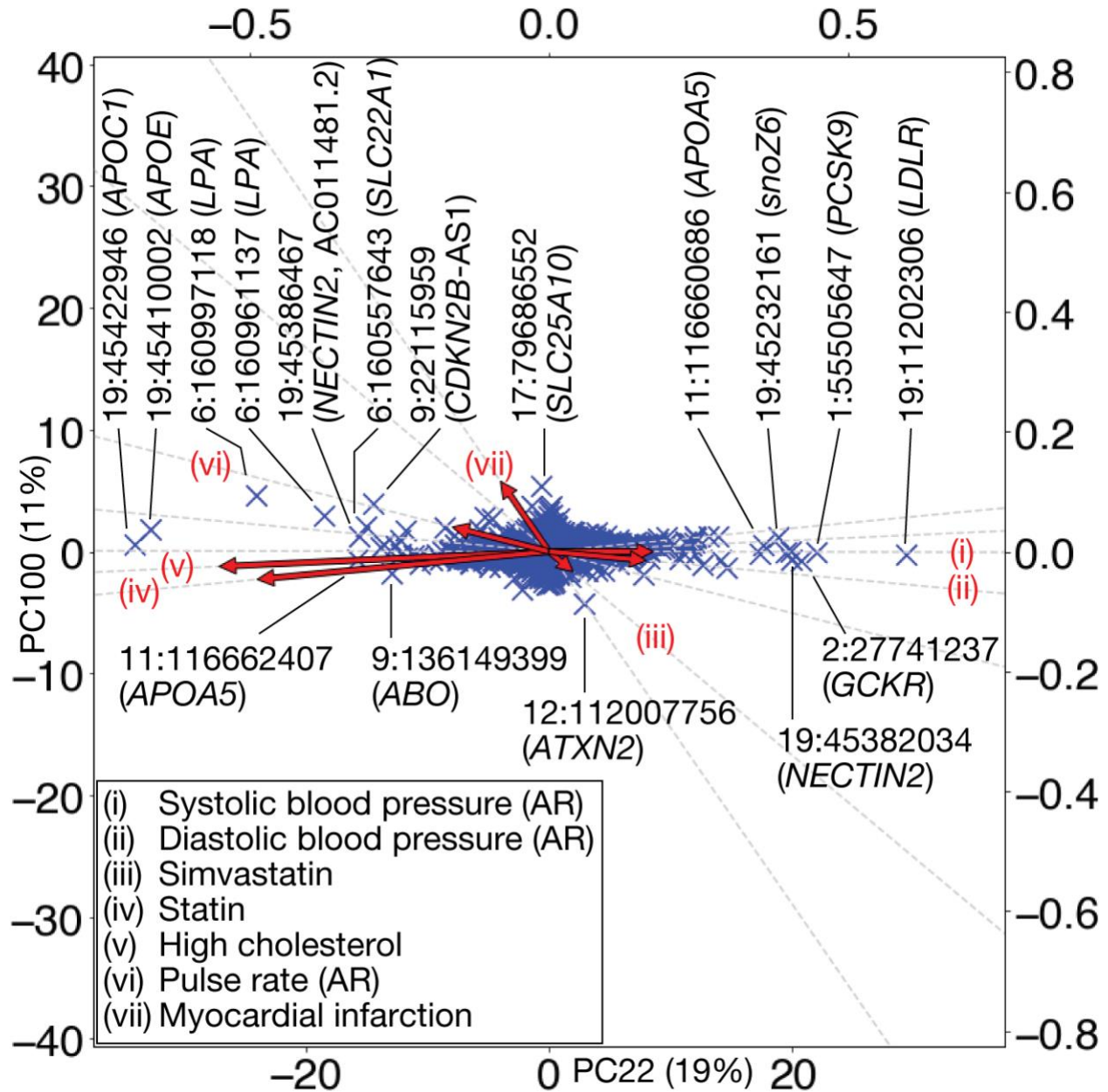
909 Fig. S4: Gene contribution score (all variants dataset)



910
 911
 912 **Fig. S4** Gene contribution scores for the top three key components for body mass index (BMI),
 913 myocardial infarction (MI), and gallstones using all variant dataset, which includes both coding
 914 and non-coding variants. For each phenotype, the top three key components with their
 915 phenotype squared cosine scores are shown on the top of the stacked bar plot and gene
 916 contribution scores for each of the components are shown as colored segments. Each colored
 917 segment represents a gene with at least 0.05% of contribution scores and the rest of the genes
 918 are aggregated as the gray bar at the top. For the visualization, the maximum value of the
 919 vertical axis is set to be 0.6. For each component, the labels for the top 10 driving genes are
 920 shown. For non-coding variants, we display their genomic coordinates.

921 Fig. S5: Variant PCA plot for myocardial infarction.

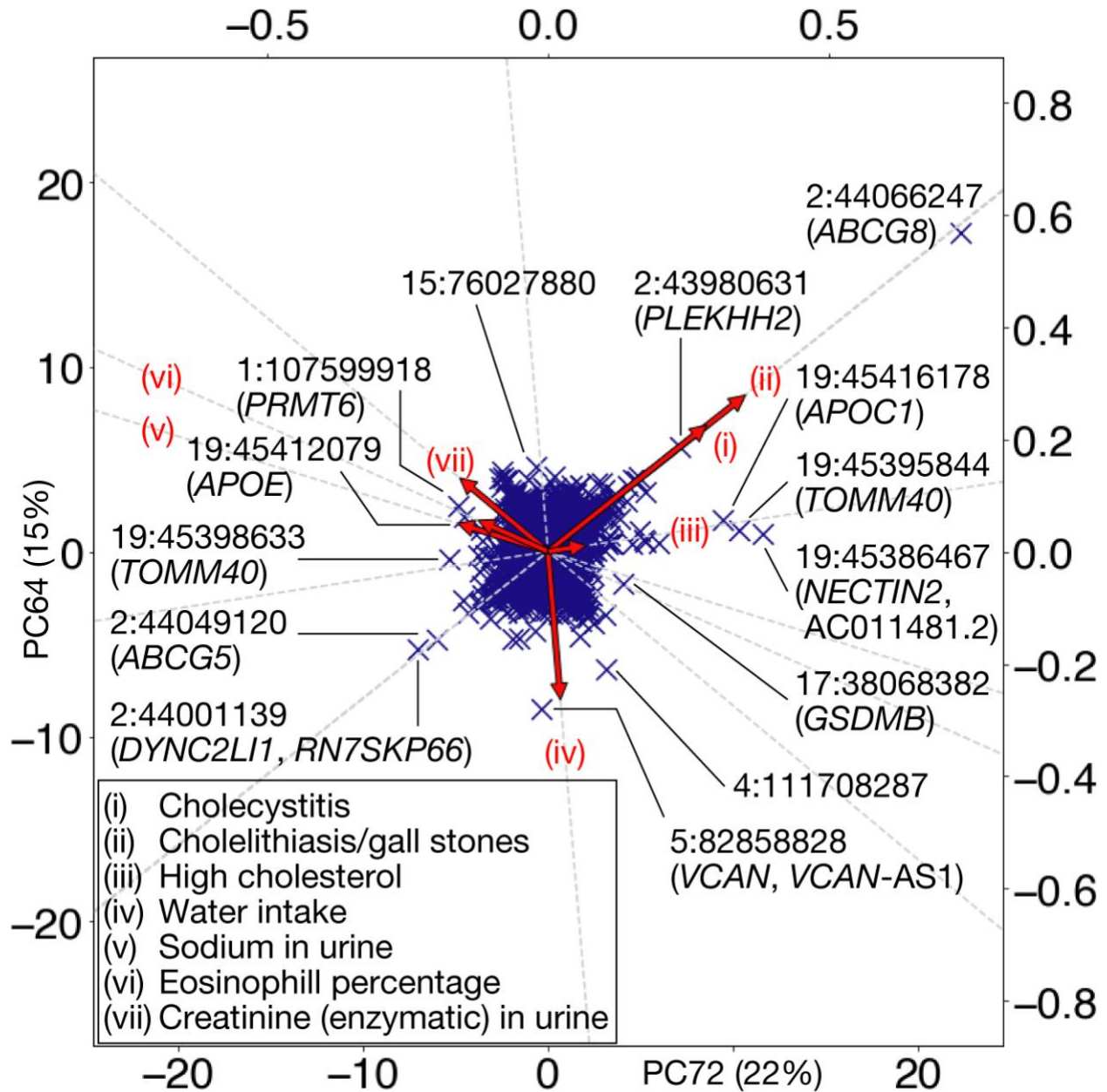
922



923

924 **Fig. S5** Variant PCA plot with biplot annotation for the top two key components for myocardial
 925 infarction using “all” dataset. Genetic variants projected into the top two key components, PC22
 926 (horizontal axis) and PC100 (vertical axis) are shown as scatter plot. Variants are annotated
 927 with gene symbols. Directions of genetic associations for relevant phenotypes are annotated as
 928 red arrows using the secondary axes (Methods). Abbreviations. AR: automated reading.

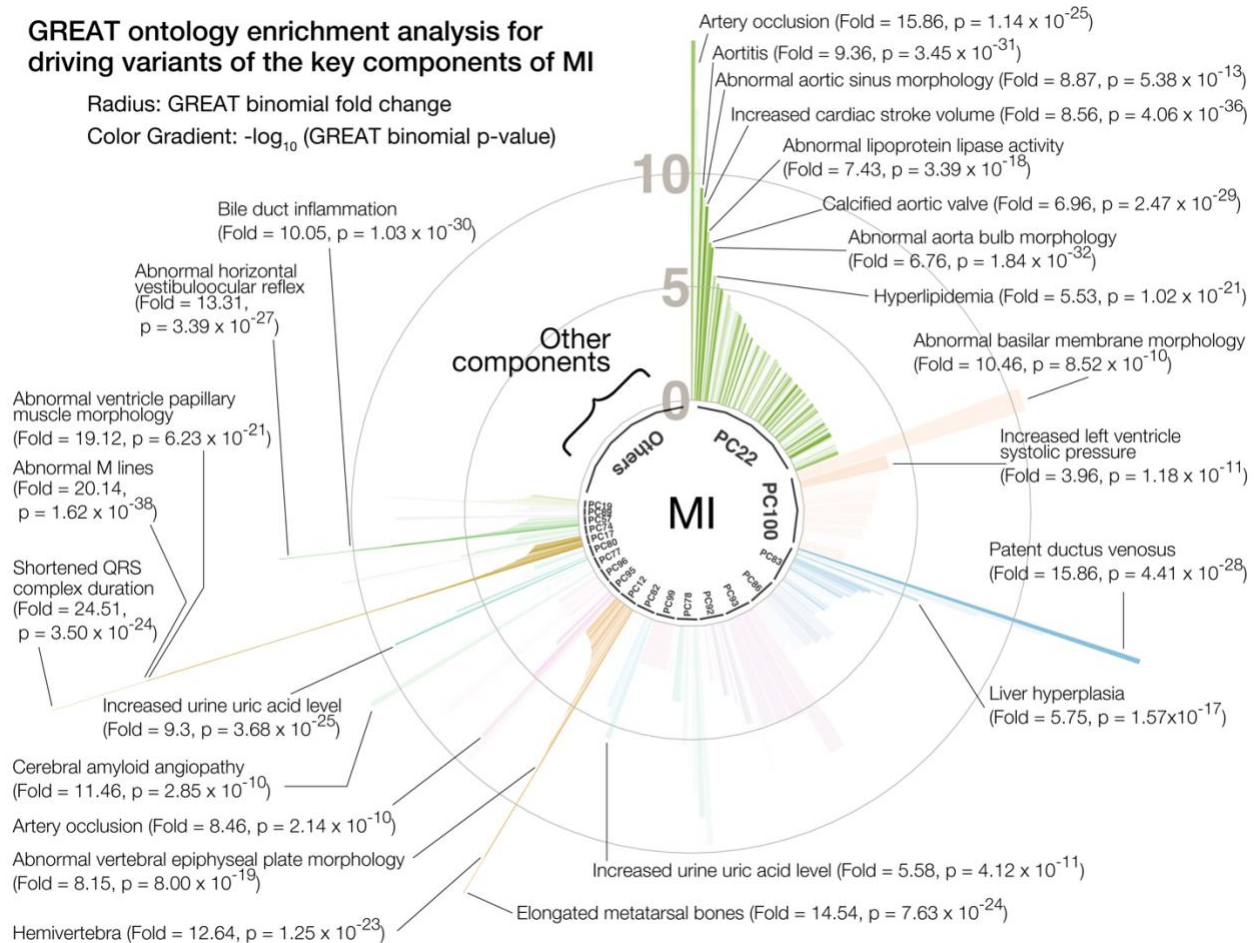
929 Fig. S6: Variant PCA plot for Gallstones



930
 931 **Fig. S6** Variant PCA plot with biplot annotation for the top two key components for gallstones
 932 using “all” dataset. Genetic variants projected into the top two key components, PC72
 933 (horizontal axis) and PC64 (vertical axis). Variants are annotated with gene symbols. Directions
 934 of genetic associations for relevant phenotypes are annotated as red arrows using the
 935 secondary axes (Methods).

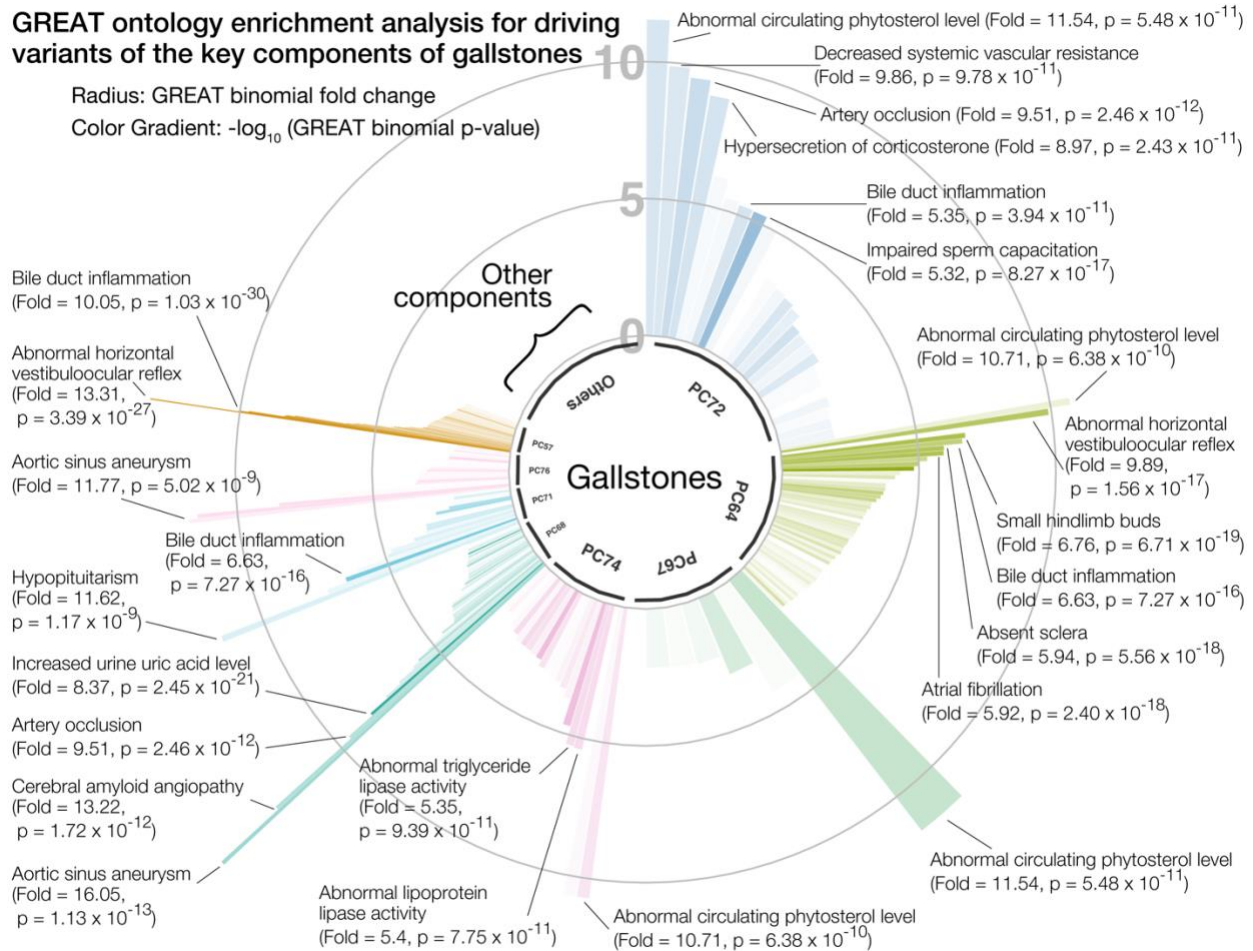
936

937 Fig. S7: GREAT enrichment analysis for MI



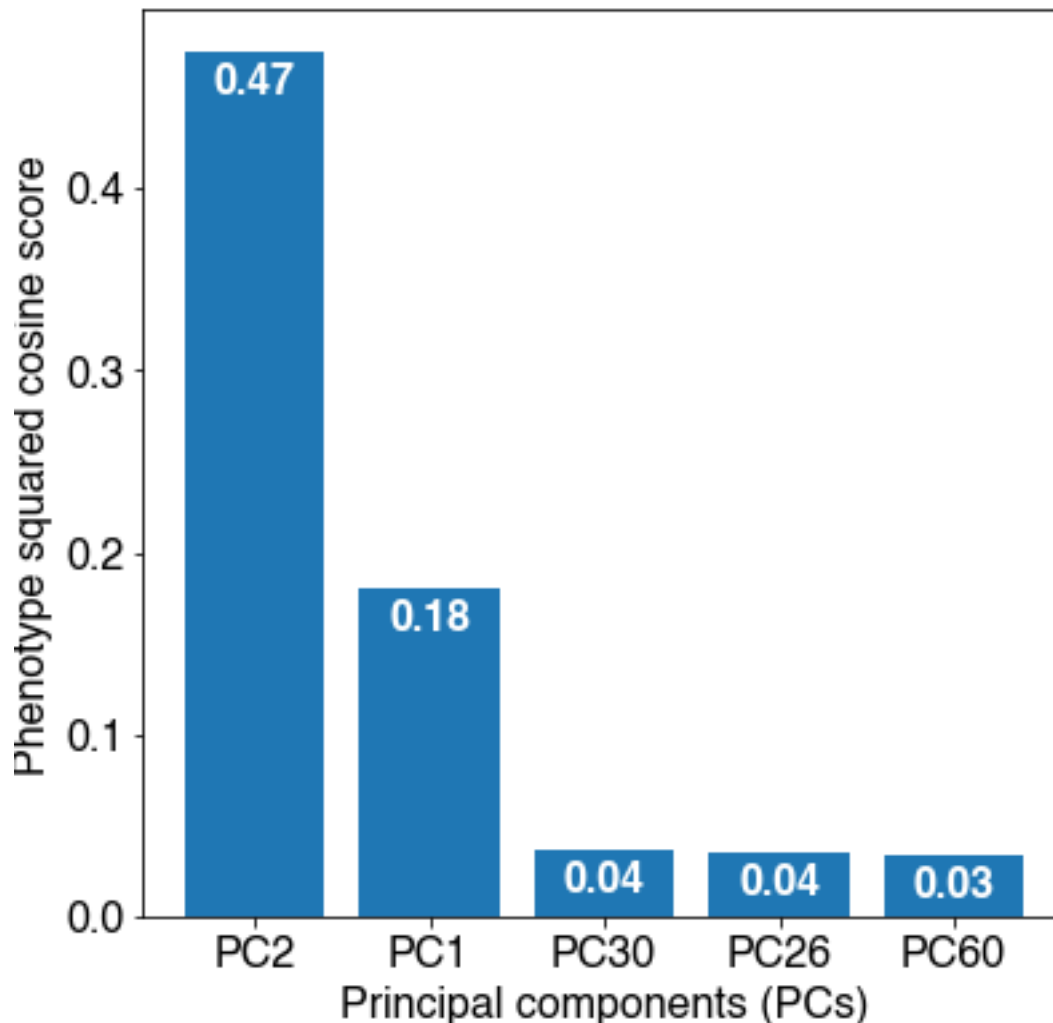
938
939 **Fig. S7** Biological characterization of driving non-coding and coding variants of the key
940 components for myocardial infarction (MI) with the genomic region enrichment analysis tool
941 (GREAT) using the all variants dataset. The key components are shown proportional to their
942 squared cosine score along with significantly enriched terms in mouse genome informatics
943 (MGI) phenotype ontology. The radius represents binomial fold change and the color gradient
944 represents p-value from GREAT ontology enrichment analysis.

945 **Fig. S8: GREAT ontology enrichment analysis for gallstones**



946
947 **Fig. S8** Biological characterization of driving non-coding and coding variants of the key
948 components for gallstones with the genomic region enrichment analysis tool (GREAT) using the
949 all variants dataset. The key components are shown proportional to their squared cosine score
950 along with significantly enriched terms in mouse genome informatics (MGI) phenotype ontology.
951 The radius represents binomial fold change and the color gradient represents p-value from
952 GREAT ontology enrichment analysis.

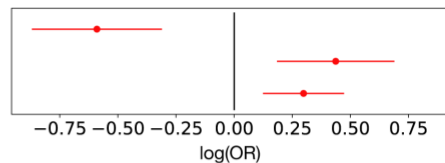
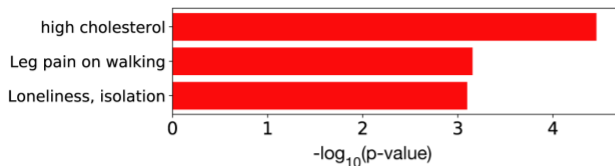
953 Fig. S9: Squared cosine score of BMI (PTVs dataset)



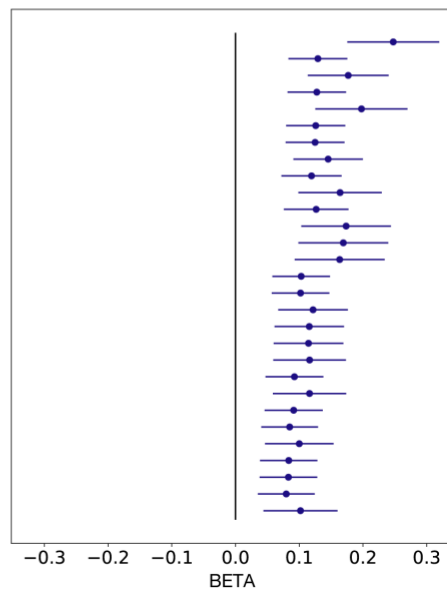
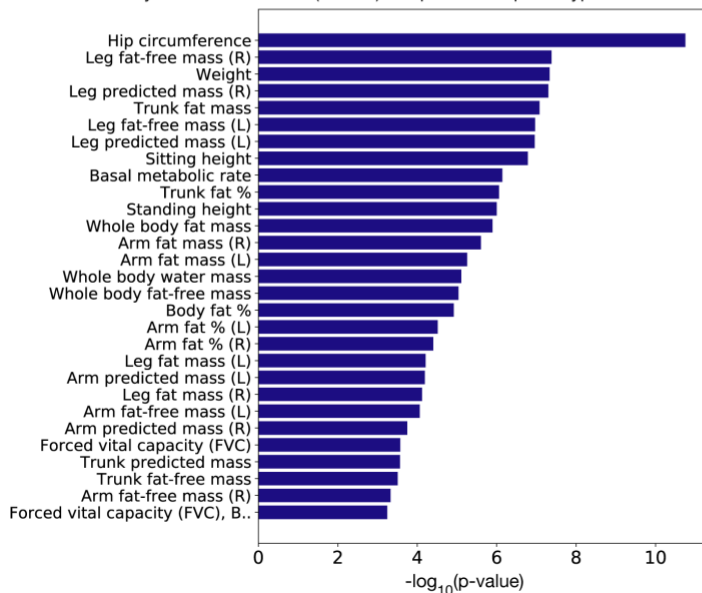
954
955 **Fig. S9** Identification of the key components for BMI with phenotype squared cosine scores
956 using the PTVs dataset. The top five key components are shown on the horizontal axis and the
957 corresponding squared cosine scores are shown on the vertical axis.

958 **Fig. S10: PheWAS analysis for *PDE3B***

a PheWAS analysis of rs150090666 (*PDE3B*) for binary phenotypes

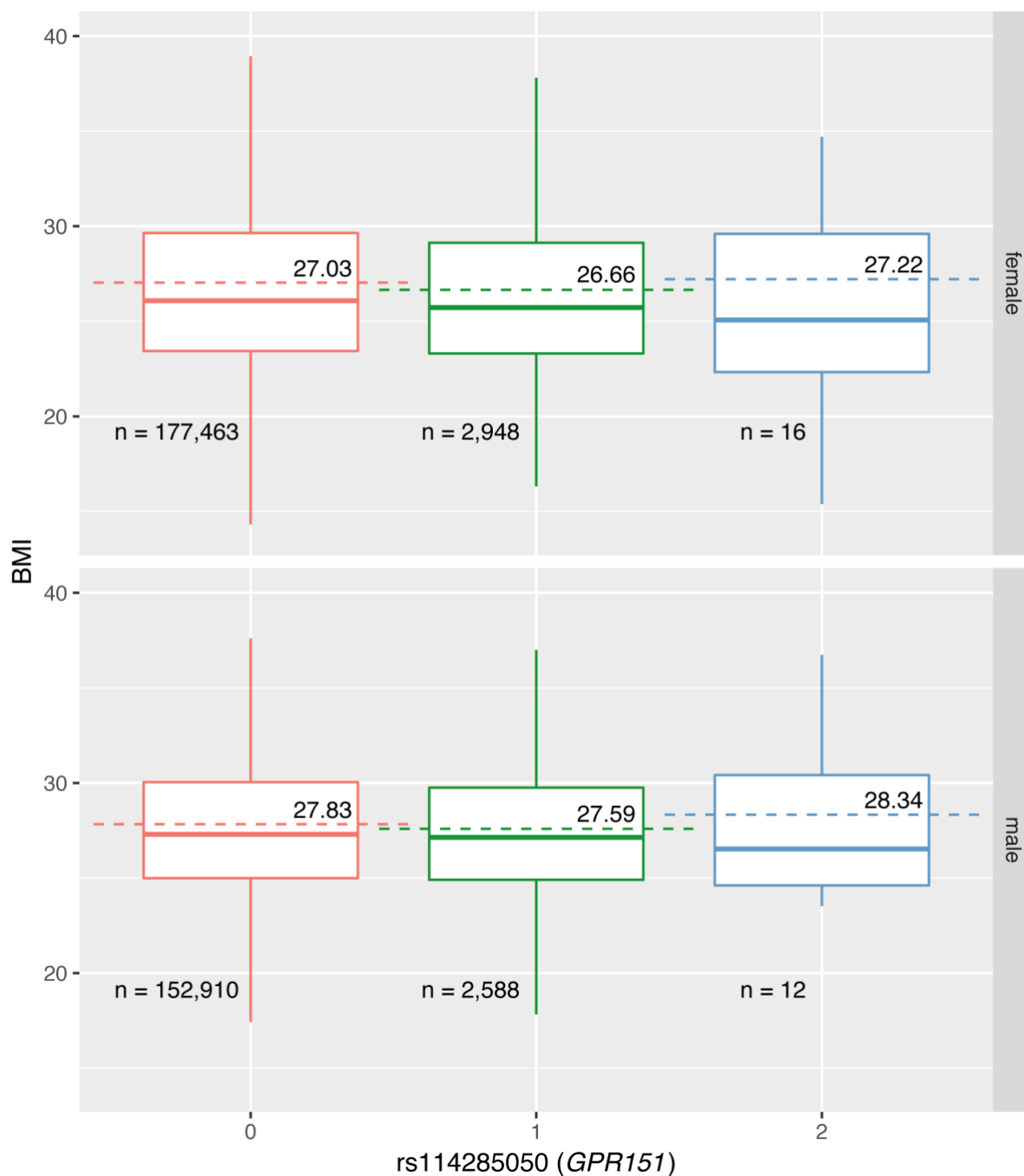


b PheWAS analysis of rs150090666 (*PDE3B*) for quantitative phenotypes



959
 960 **Fig. S10** Phenome-wide association (PheWAS) analysis for rs150090666, a stop-gain variant in
 961 *PDE3B*. The p-values (left) and log odds ratio (binary phenotypes, shown as red)
 962 (quantitative phenotypes, shown as blue) (right) along with 95% confidence interval are shown
 963 for the phenotypes with minimum case count of 1,000 (binary phenotypes, **a**) or 1,000
 964 individuals with non-missing values (quantitative phenotypes, **b**) and strong association ($p \leq$
 965 0.001) and with this variants among all the phenotypes used in the study.

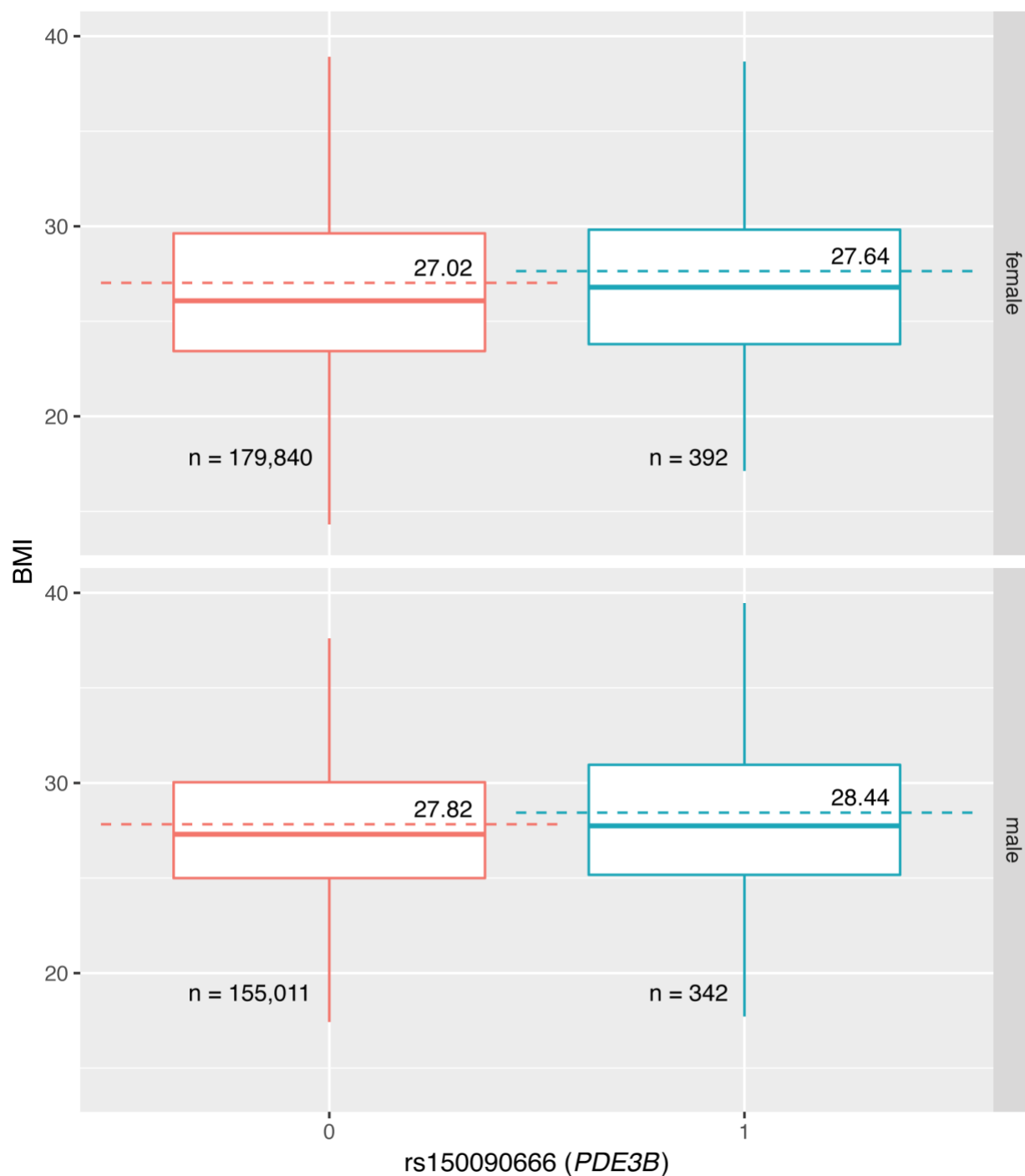
966 Fig. S11: Univariate regression analysis for *GPR151*



967
968
969
970
971
972

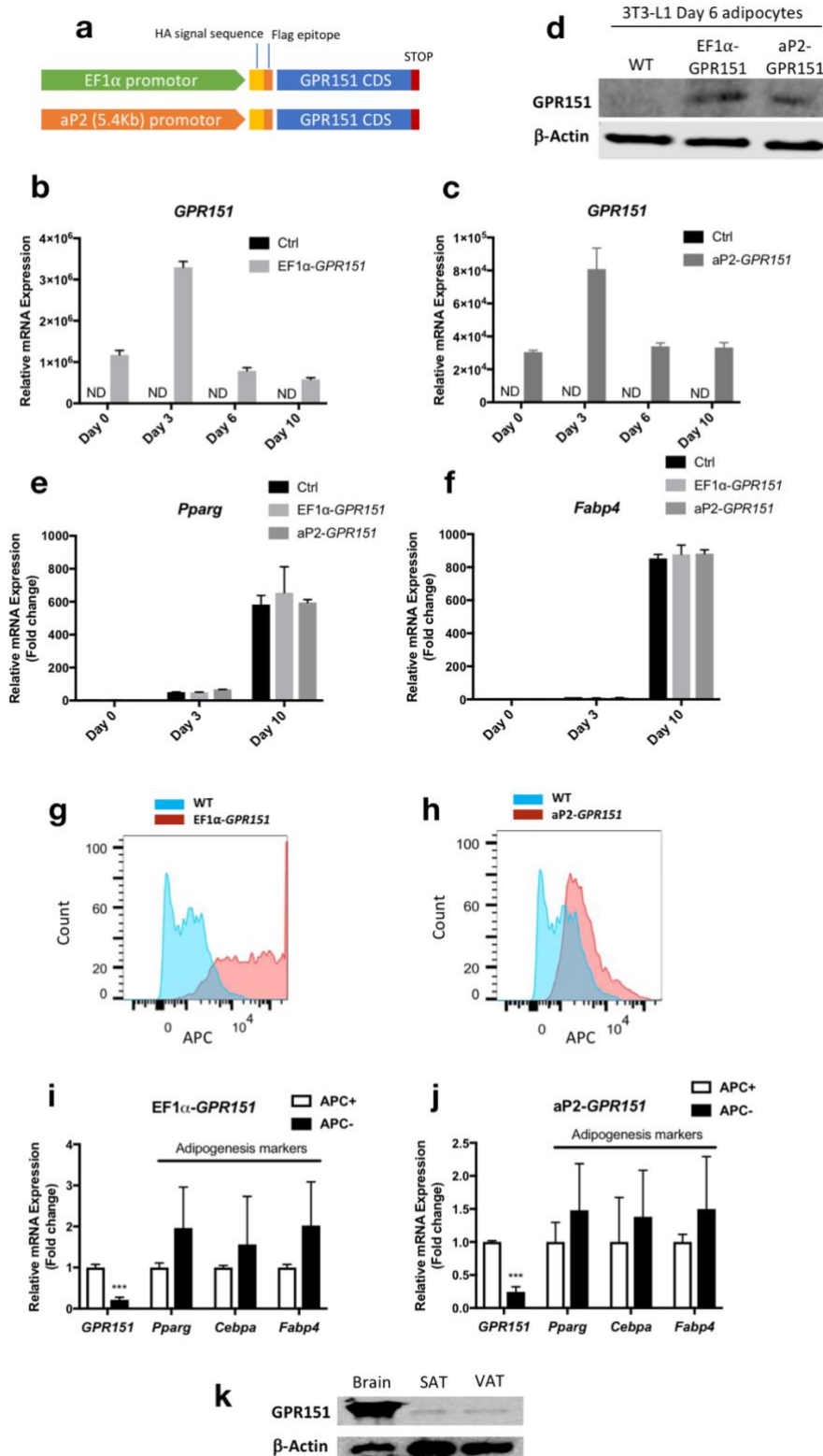
Fig. S11 Distribution of BMI stratified by sex and genotype of rs114285050, a stop-gain variant in *GPR151*. The outliers are removed from the plot and the mean values are annotated and shown as dashed lines. The number of carriers of the variants are shown at the bottom.

973 Fig. S12: Univariate regression analysis for *PDE3B*



974
975 **Fig. S12** Distribution of BMI stratified by sex and genotype of rs150090666, a stop-gain variant
976 in *PDE3B*. The outliers are removed from the plot and the mean values are annotated and
977 shown as dashed lines. The number of carriers of the variants are shown at the bottom.
978

979 Fig. S13: *GPR151* overexpression

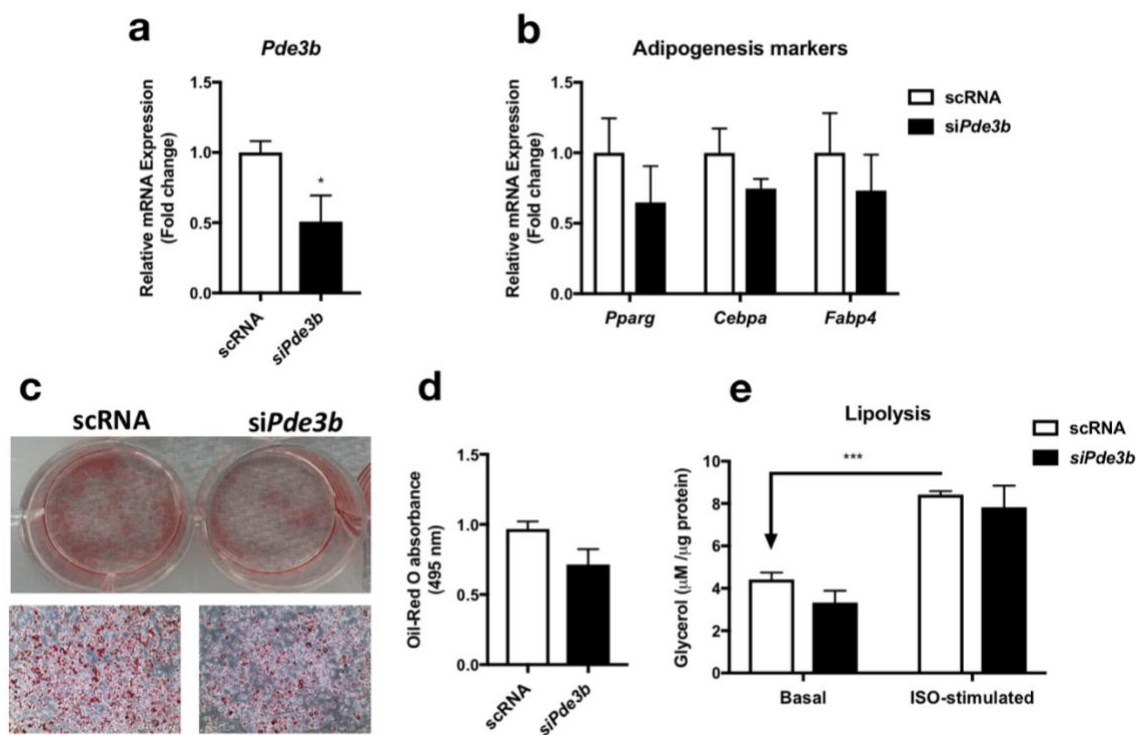


980
 981
 982

Fig. S13 Effects of *GPR151* overexpression on 3T3-L1 adipogenesis. **a** Structure of *GPR151* overexpression construct driven by either EF1 α or aP2 promoter. **b-d** Confirmation of *GPR151*

983 overexpression at both mRNA (b-c) and protein levels (d) in 3T3-L1 cells during adipogenesis.
984 e-f qPCR analysis of the effect of *GPR151* overexpression on adipogenesis markers, *Pparg* (e)
985 and *Fabp4* (f). g-h FACS analysis of APC fluorescence in Day 6 3T3-L1 adipocytes infected
986 with either EF1 α -*GPR151* (g) or aP2-*GPR151* (h) (shown in red), in comparison to wild-type
987 (WT) cells (shown in blue). i-j Relative mRNA levels of *GPR151* and adipogenic markers
988 (*Pparg*, *Cebpa*, *Fabp4*) in purified APC+ and APC- cells from Day 6 3T3-L1 adipocytes infected
989 by either EF1 α -*GPR151* (i) or aP2-*GPR151* (j). k Comparison of protein levels of *GPR151* in
990 mouse brain, subcutaneous adipose tissue (SAT) and visceral adipose tissue (VAT). ND: not-
991 detectable.
992

993 Fig. S14: *Pde3b* knockdown



994 **Fig. S14** Effects of *Pde3b* knockdown in 3T3-L1 adipogenesis. **a** qPCR analysis of *Pde3b*
995 mRNA knockdown in 3T3-L1 preadipocytes. **b** qPCR analysis of the effect of si*Pde3b*
996 knockdown on adipogenesis markers, *Pparg*, *Cebpa* and *Fabp4*. **c-d** Oil-Red O staining (**c**) and
997 quantification (**d**) of lipid droplets in scRNA- or si*Pde3b*-transfected adipocytes. **e** lipolysis
998 assays of scRNA- or si*Pde3b*-transfected adipocytes. Means \pm SEM are shown (**p-
999 value<0.001, *p-value<0.05). scRNA: scrambled siRNA. ISO: isoproterenol.
1000

1001 **Table S1 List of phenotype categories**

1002 List of phenotype categories used in our study and their data source are shown with one
 1003 example phenotype per category. Abbreviation in the type column. B: binary, Q: quantitative, P:
 1004 described in previously published literature, F: the UK Biobank data field ID, and C: the UK
 1005 Biobank data category ID.

1006

Phenotype group name	Type	Number of phenotypes	Example	Data source
Disease outcome	B	363	Hypertension	P ¹²
Cancer	B	46	Skin cancer	P ¹²
Family History	B	10	High blood pressure	P ¹²
Medication	B	709	Aspirin intake	F:20003
Questionnaire (binary)	Q	49	Wears glasses or contact lenses	C:100025
Imaging	Q	683	Volume of white matter	C:100003
Physical Measurement	Q	122	Standing height	C:100006
Assay	Q	34	Red blood cell (erythrocyte) count	C:100079
Questionnaire (quantitative)	Q	62	Sleep duration	C:100079
Miscellaneous (binary)	B	19	Ever attempted suicide	
Miscellaneous (quantitative)	Q	42	Number of medications taken	

1007

1008 Table S2 List of phenotypes

1009 The list of phenotypes considered in the study. The table is sorted by category, number cases
 1010 (for binary phenotypes), and the number of non-missing values (for quantitative phenotypes).
 1011 The two columns, "All" and "PTVs" indicates whether the phenotype is used in each of the
 1012 dataset after imposing the filters on the genome-and phenome-wide summary statistics matrix.
 1013 One can browse the summary statistics from genome-wide association studies on the Global
 1014 Biobank Engine with the URL in the table.

1015 I am showing the first five lines of the table here. The full table is in Excel file.

Category	Phenotype name	Number of cases	All	PTVs	Global Biobank Engine phenotype page (URL)
Disease outcome	hypertension	107407	Y	Y	https://biobankengine.stanford.edu/coding/HC215
Disease outcome	essential hypertension	64234	Y	Y	https://biobankengine.stanford.edu/coding/HC273
Disease outcome	asthma	43626	Y	Y	https://biobankengine.stanford.edu/coding/HC382
Disease outcome	high cholesterol	43054	Y	Y	https://biobankengine.stanford.edu/coding/HC269

1016

1017 Table S3: Phenotype groupings for visualization

1018 The list of phenotype groups used in the phenotype contribution score plots are summarized.

Phenotype groups	List of phenotypes in the group
fat-free	Arm fat-free mass (left)
	Arm fat-free mass (right)
	Leg fat-free mass (left)
	Leg fat-free mass (right)
	Total fat-free mass
	Trunk fat-free mass
	Whole body fat-free mass
fat	Android fat mass
	Android tissue fat percentage
	Arm fat mass (left)

	Arm fat mass (right)
	Arm fat percentage (left)
	Arm fat percentage (right)
	Arm tissue fat percentage (left)
	Arm tissue fat percentage (right)
	Arms fat mass
	Arms tissue fat percentage
	Body fat percentage
	Gynoid fat mass
	Gynoid tissue fat percentage
	Leg fat mass (left)
	Leg fat mass (right)
	Leg fat percentage (left)
	Leg fat percentage (right)
	Leg tissue fat percentage (left)
	Leg tissue fat percentage (right)
	Legs fat mass
	Legs tissue fat percentage
	Total fat mass
	Total tissue fat percentage
	Trunk fat mass
	Trunk fat percentage
	Trunk tissue fat percentage
	Whole body fat mass
impedance	Impedance of arm (left)
	Impedance of arm (right)

	Impedance of leg (left)
	Impedance of leg (right)
	Impedance of whole body
reticulocyte	High light scatter reticulocyte count
	High light scatter reticulocyte percentage
	Immature reticulocyte fraction
	Mean reticulocyte volume
	Reticulocyte count
	Reticulocyte percentage
meridian	3mm strong meridian (left)
	3mm strong meridian (right)
	3mm weak meridian (left)
	3mm weak meridian (right)
	6mm strong meridian (left)
	6mm strong meridian (right)
	6mm weak meridian (left)
	6mm weak meridian (right)
spirometry	Forced expiratory volume in 1-second (FEV1)
	Forced expiratory volume in 1-second (FEV1), Best measure
	Forced expiratory volume in 1-second (FEV1), predicted
	Forced expiratory volume in 1-second (FEV1), predicted percentage
	Forced vital capacity (FVC)
	Forced vital capacity (FVC), Best measure
	Peak expiratory flow (PEF)

1020 **Table S4: Summary of contribution scores for the key**
 1021 **components**

1022 The list of top 20 driving phenotypes, genes, and variants for the first five principal components
 1023 and the top three key components for the phenotypes highlighted in the study are summarized
 1024 in the table.

1025 I am showing the first four lines of the table here. The full table is in Excel file.

Dataset	Phenotype of interest	PC	Squared cosine score	Rank	Phenotype	Phenotype contribution score	Gene	Gene contribution score	Variant	Variant contribution score	rsid	GBE
All_variants	BMI	2	47.44%	1	Standing height	9.51%	FTO	1.52%	16-53813367	0.97%	rs178174	https://biobankengine.stanford.edu/variant/16-53813367
All_variants	BMI	2	47.44%	2	Arm fat percentage (left)	5.76%	ADCY3	0.31%	16-53826034	0.28%	rs718796	https://biobankengine.stanford.edu/variant/16-53826034
All_variants	BMI	2	47.44%	3	Body fat percentage	5.64%	DNMT3A	0.30%	2-417167	0.27%	rs621062	https://biobankengine.stanford.edu/variant/2-417167

1026

1027 **Table S5: GREAT enrichment analysis for BMI**

1028 Biological characterization of driving non-coding and coding variants of the key components for
 1029 BMI with the genomic region enrichment analysis tool (GREAT) using the all variants dataset.

1030 The results of the enrichment analysis for MGI phenotype ontology, a manually curated
 1031 genotype-phenotype relationship knowledgebase for mouse, is summarized by the key
 1032 components. The two major summary statistics from GREAT, binomial fold and binomial p-
 1033 value, are shown. Abbreviation. BFold: binomial fold, BPval: binomial p-value.

1034 Here, I'm showing the first 3 lines of the table. The full table is in Excel file.

PC rank	PC	Term	BFold	BPval
1	PC2	brachypodia	9.05	1.40E-23
1	PC2	abnormal pancreas topology	8.13	8.80E-12
1	PC2	abnormal urine catecholamine level	7.32	5.19E-18

1035 **Table S6: GREAT enrichment analysis for MI**

1036 Biological characterization of driving non-coding and coding variants of the key components for
 1037 MI with the genomic region enrichment analysis tool (GREAT) using the all variants dataset.

1038 The results of the enrichment analysis for MGI phenotype ontology, a manually curated

1039 genotype-phenotype relationship knowledgebase for mouse, is summarized by the key
 1040 components. The two major summary statistics from GREAT, binomial fold and binomial p-
 1041 value, are shown. Abbreviation. BFold: binomial fold, BPval: binomial p-value.

1042 **Here, I'm showing the first 3 lines of the table. The full table is in Excel file.**

PC rank	PC	Term	BFold	BPval
1	PC22	artery occlusion	1.59E+01	1.14E-25
1	PC22	aortic sinus aneurysm	1.28E+01	3.88E-10
1	PC22	abnormal circulating phytosterol level	1.07E+01	6.38E-10

1043 Table S7: GREAT enrichment analysis for gallstones

1044 Biological characterization of driving non-coding and coding variants of the key components for
 1045 gallstones with the genomic region enrichment analysis tool (GREAT) using the all variants
 1046 dataset. The results of the enrichment analysis for MGI phenotype ontology, a manually curated
 1047 genotype-phenotype relationship knowledgebase for mouse, is summarized by the key
 1048 components. The two major summary statistics from GREAT, binomial fold and binomial p-
 1049 value, are shown. Abbreviation. BFold: binomial fold, BPval: binomial p-value.

1050 **Here, I'm showing the first 3 lines of the table. The full table is in Excel file.**

PC rank	PC	Term	BFold	BPval
1	PC72	abnormal circulating phytosterol level	1.15E+01	5.48E-11
1	PC72	decreased systemic vascular resistance	9.86E+00	9.78E-11
1	PC72	artery occlusion	9.51E+00	2.46E-12

1051 Table S8: PheWAS analysis for rs114285050 (*GPR151*)

1052 Phenome-wide association (PheWAS) analysis for rs114285050, a stop-gain variant in
 1053 *GPR151*.

GBE phenotype code	Name	Case	-log ₁₀ p-value	log(OR) or Beta	1.96 * SE(log(OR)) or 1.96 * SE(beta)
BIN1960	Fed-up feelings	136434	3.041	-0.09304	0.054978
INI48	Waist circumference	336659	7.599	-0.06544	0.02301
INI23100	Whole body fat mass	330970	6.87	-0.06872	0.025539
INI23128	Trunk fat mass	331295	6.835	-0.07053	0.026284
INI23120	Arm fat mass (right)	331422	6.816	-0.06863	0.025617
INI23099	Body fat percentage	331318	6.816	-0.05306	0.019816

INI23127	Trunk fat percentage	331314	6.79	-0.06356	0.023775
INI21002	Weight	336260	6.654	-0.06087	0.02303
INI23116	Leg fat mass (left)	331470	6.649	-0.05468	0.020698
INI23112	Leg fat mass (right)	331488	6.62	-0.05517	0.020933
INI21001	Body mass index (BMI)	336144	6.498	-0.06789	0.026029
INI23111	Leg fat percentage (right)	331491	6.341	-0.04201	0.016327
INI23124	Arm fat mass (left)	331362	6.317	-0.06587	0.025656
INI23115	Leg fat percentage (left)	331473	6.17	-0.04087	0.016123
INI23119	Arm fat percentage (right)	331445	5.424	-0.04689	0.019874
INI23123	Arm fat percentage (left)	331395	5.048	-0.04485	0.019796
INI49	Hip circumference	336620	4.649	-0.05669	0.026205
INI23126	Arm predicted mass (left)	331345	4.211	-0.03373	0.016499
INI23125	Arm fat-free mass (left)	331358	3.929	-0.03257	0.01658
INI23105	Basal metabolic rate	331502	3.923	-0.03368	0.017154
INI23117	Leg fat-free mass (left)	331454	3.423	-0.03063	0.016887
INI23118	Leg predicted mass (left)	331449	3.336	-0.02998	0.016776
INI23121	Arm fat-free mass (right)	331418	3.32	-0.02894	0.016241
INI23122	Arm predicted mass (right)	331413	3.176	-0.02808	0.016174
INI23102	Whole body water mass	331510	3.044	-0.02784	0.01644
INI23114	Leg predicted mass (right)	331480	3.019	-0.02812	0.016689

1054

1055 **Table S9: PheWAS analysis for rs150090666 (*PDE3B*)**

1056 Phenome-wide association (PheWAS) analysis for rs150090666, a stop-gain variant in *PDE3B*.

1057

GBE phenotype code	Name	Case	-log₁₀ p-value	log(OR) or Beta	1.96 * SE(log(OR)) or 1.96 * SE(beta)
HC269	high cholesterol	43054	4.457	-0.5904	0.279692
BIN4728	Leg pain on walking	28151	3.154	0.4366	0.252448
BIN2020	Loneliness, isolation	60153	3.098	0.2983	0.174322
INI49	Hip circumference	336620	10.75	0.2476	0.072167

INI23113	Leg fat-free mass (right)	331480	7.381	0.1293	0.046197
INI21002	Weight	336260	7.333	0.1769	0.063445
INI23114	Leg predicted mass (right)	331480	7.3	0.1276	0.045884
INI23128	Trunk fat mass	331295	7.079	0.1977	0.072304
INI23117	Leg fat-free mass (left)	331454	6.965	0.1259	0.046432
INI23118	Leg predicted mass (left)	331449	6.958	0.1249	0.046119
INI20015	Sitting height	336513	6.783	0.1454	0.054449
INI23105	Basal metabolic rate	331502	6.141	0.1193	0.047177
INI23127	Trunk fat percentage	331314	6.059	0.1641	0.065405
INI50	Standing height	336500	6	0.1266	0.050725
INI23100	Whole body fat mass	330970	5.895	0.1736	0.070227
INI23120	Arm fat mass (right)	331422	5.601	0.1692	0.070462
INI23124	Arm fat mass (left)	331362	5.255	0.1635	0.070521
INI23102	Whole body water mass	331510	5.107	0.1031	0.045198
INI23101	Whole body fat-free mass	331486	5.039	0.1021	0.045119
INI23099	Body fat percentage	331318	4.919	0.1217	0.054508
INI23123	Arm fat percentage (left)	331395	4.516	0.1158	0.054429
INI23119	Arm fat percentage (right)	331445	4.401	0.1146	0.054645
INI23116	Leg fat mass (left)	331470	4.208	0.1163	0.056918
INI23126	Arm predicted mass (left)	331345	4.189	0.09246	0.045374
INI23112	Leg fat mass (right)	331488	4.119	0.1162	0.057565
INI23125	Arm fat-free mass (left)	331358	4.061	0.09128	0.04559
INI23122	Arm predicted mass (right)	331413	3.746	0.085	0.044472
INI3062	Forced vital capacity (FVC)	309028	3.572	0.1001	0.053841
INI23130	Trunk predicted mass	331203	3.565	0.08357	0.045002
INI23129	Trunk fat-free mass	331234	3.508	0.08307	0.045158
INI23121	Arm fat-free mass (right)	331418	3.326	0.07965	0.044649
INI20151	Forced vital capacity (FVC), Best measure	255494	3.243	0.102	0.058016